Investigation of in-liquid ordering mediated transformations in Al-Sc via *ab initio* molecular dynamics and unsupervised learning

Deep Choudhuri [ORCID],[*] Bhaskar S. Majumdar, and Hunter Wilkinson [ORCID]

Department of Materials and Metallurgical Engineering, New Mexico Institute of Mining and Technology, Socorro, New Mexico, 87801, USA

Scandium is well known to produce grain refinement in Al-based alloys, and its potency is generally attributed to intermetallic Al_3Sc formation within liquid phase. However, the influence of Sc atoms and Al_3Sc on the local structure of the surrounding melt, and subsequent nucleation remains unclear. Towards that end, we have probed structural changes in three bulk compositions, i.e., Al-*x*Sc (x = 0, 0.4, 1.0 at.%), and near liquid-Al/Al_3Sc interfacial regions using *ab initio* molecular dynamics. In-liquid ordering was determined using unsupervised learning techniques, i.e., structural fingerprinting, dimensionality reduction, and cluster analysis. Sc atoms ordered the surrounding liquid Al atoms by forming Sc-centered polyhedrons, while liquid-Al/Al_3Sc interface manifested planar ordering that resembled $\{100\}_{fcc-Al}$. Both structures were geometrically persistent but constitutionally transient, i.e., they exchanged Al atoms with the surrounding liquid. This behavior was rationalized on the basis of their mixed metallic and covalent bond character. At a lower temperature, $\{100\}_{fcc-Al}$ interfacial planes heteroepitaxially nucleated equilibrium fcc-Al, while Sc-centered polyhedrons sequentially formed metastable *hcp*- and *bcc*-Al. Using our simulations and extant experimental reports, we postulate two transformation pathways during Al-Sc solidification: (i) $Sc-centered\ polyhedrons \rightarrow Al_3Sc \rightarrow liquid-Al/Al_3Sc\ interfacial\ ordering \rightarrow fcc-Al$; and (ii) $Sc-centered\ polyhedrons \rightarrow hcp-Al \rightarrow bcc-Al \rightarrow fcc-Al$. The two in-liquid ordered structures provide an atomistic basis for the potency of Sc element, and, also, serve as possible structural metrics for designing novel Al-based alloys.

I. INTRODUCTION

Liquid state of many materials contain nanoscale ordered domains embedded within bulk disordered regions, and those domains are known to influence nucleation of crystalline phases [1–7]. Studies on metallic alloys showed that in-liquid ordered domains can take the form of 3D polyhedral cage-like structures that resemble icosahedrons with fivefold symmetry (space group $m\bar{3}\bar{5}$) [2–7]. Such structures facilitate the formation of crystallographically complex intermetallic compounds [8–14], and simpler face-centered-cubic (fcc) [3,4]—a common structure present in many commercial alloys. However, a large body of literature shows that the homogeneous nucleation of equilibrium fcc within a liquid phase is initiated by intermediary metastable phases like body-centered-cubic (*bcc*), and, in limited cases, hexagonal-closed-packed (*hcp*) [15–23]. Therefore, it is unclear how such metastable structures and in-liquid ordered domains interact with each other to form equilibrium fcc. Towards that end, we probed atomicscale structural changes during the solidification of binary Al-Sc alloys, by employing *ab initio* molecular dynamics (AIMD) simulations and unsupervised machine learning.

The solidified microstructures of high-strength engineering Al-Sc-based alloys comprise fcc-Al grains and intermetallic fcc-ordered Al_3Sc (space group $P\frac{4}{m}\bar{3}\frac{2}{m}$ and *strukturbericht* $L1_2$) [24,25]. In such Al-based systems, Sc is considered a potent grain refiner due to Al_3Sc formation within alloy melt [26–29]. Detailed microstructure characterization of Al-Sc alloys have suggested that Al_3Sc facilitates heterogeneous nucleation of fcc-Al [26–29]. Interestingly, a mechanistic basis of such Al_3Sc-mediated fcc-Al nucleation remains unexplored. Furthermore, a recent experimental study has suggested that Sc-centered polyhedrons act as precursors to Al_3Sc formation [14]. Therefore, it is conceivable that such polyhedrons may affect fcc-Al nucleation in Al-Sc systems. Broadly, a mechanistic assessment of structural changes during Al-Sc solidification will provide vital insights into the potency of Sc as a grain refiner, and inform approaches for designing new engineering alloys.

Regardless of the geometry of in-liquid ordered structures, facets on a 3D structure can initiate nucleation via "condensation" of atoms on its surface that commensurate with local crystallography, e.g., in-liquid ordering of {111}-Al on {111}-MgO [30], and the basal planes of α-Al_2O_3 [31]. Extant literature shows that such atomicscale agglomeration tends to occur within picoseconds [16–18,20–23,32]. A time-resolved observation of such a mechanism is experimentally nontrivial, because it requires *in situ* testing using dedicated, custom-built instrumentation [14,31,33,34]. However, AIMD can resolve structural changes within subpicosecond time scales [30,35–39], which enable us to probe transformation pathways mediated by in-liquid ordered structures in Al-Sc alloys.

Typically, structures present within an atomistic simulation volume are extracted by postprocessing Cartesian atomic positions via well-documented techniques, e.g., bond order
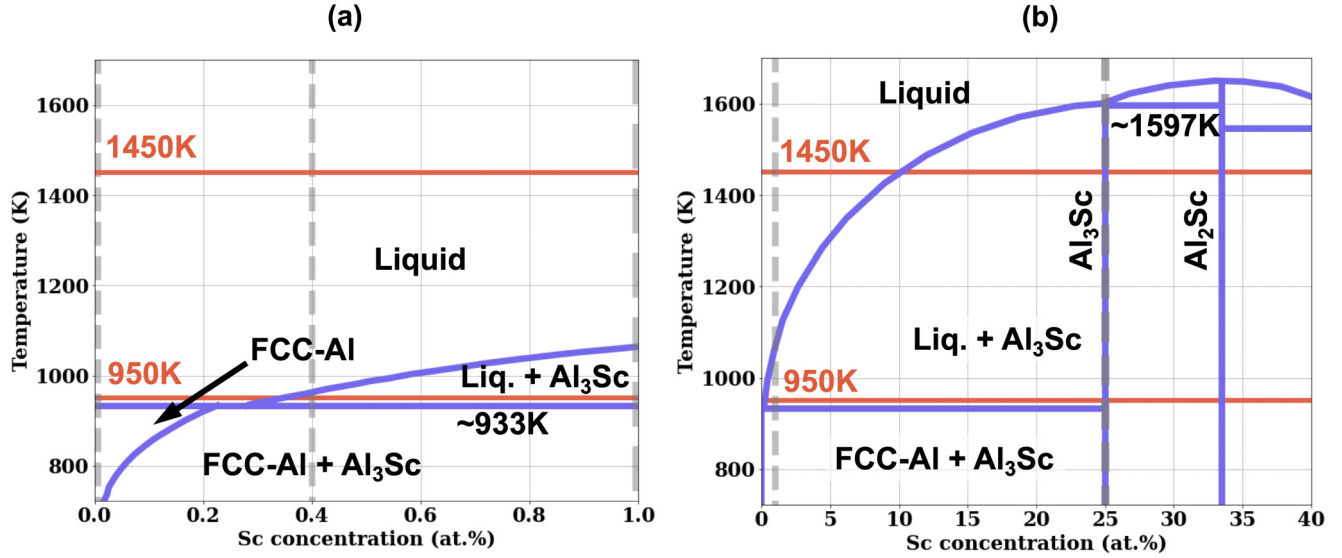
---

[*]deep.choudhuri@nmt.edu

FIG. 1. Reproduction of binary Al-Sc phase diagram from [66]. (a) Al-rich corner showing the eutectic point at ∼0.27 at.% Sc; and (b) location of Al_3Sc intermetallic line compound, and its corresponding phase domains within Al-lean regime. Annealing temperatures are indicated using red lines.

parameters, atomic density profiles, common neighbor analysis, polyhedral template matching, Voronoi tessellation, visual inspection, etc., [6,12,19,23,30,40–44]. In recent years, structure detection capabilities have been augmented through the application of machine learning techniques. Unsupervised learning (UL)—a category of machine learning—is shown to autonomously detect structure and contribute towards uncovering novel phase transformation pathways [36,45–49]. Few examples of UL approaches are dimensionality reduction, e.g., principle component analysis, t-distributed stochastic neighbor embedding (t-SNE), etc., cluster analysis, e.g., Gaussian mixture, density-based spatial clustering of applications with noise (DBSCAN), etc., neural network-based latent representation, e.g., autoencoders, variational auto encoders, and the like [36,45,50–61]. An effective application of machine learning to atomistic simulations requires the conversion of 3D Cartesian position of atoms into an invariant representation, i.e., independent of rotation and translation [47], which is also called structural fingerprinting. This approach departs from traditional approaches that use Cartesian coordinates for identifying structures. Structural fingerprinting "projects" 3D atomic positions to a multidimensional space, which machine learning algorithms can later utilize to identify unique environments within a bulk structure [47]. In this paper, we have used structural finger printing, t-SNE, and DBSCAN to detect in-liquid ordering within liquid Al-Sc.

Remainder of the paper is organized as follows: Computational protocols are presented in Sec. II, results are described in Sec. III, and, in Sec. IV, we rationalize our results and discuss their implications.

II. COMPUTATIONAL METHODS

A. Simulation methodology and initial configurations

Ab inito molecular dynamics (AIMD) was performed using the Vienna *Ab initio* Simulation Package (VASP) that employs projector augmented plane-wave (PAW) method

and computes time evolution of atomic coordinates using Born-Oppenheimer approximation [62–65]. The equations of motion was solved using Verlet's algorithm and time step 0.005 picoseconds (ps) or 5×10^{-15} s. All simulations were performed using NVT canonical ensemble, i.e., constant number of particles (N), volume (V), and temperature (T). Temperature was controlled via Nose-Hoover thermostat, and simulation box volume was constrained to achieve a nominal external pressure of ∼0 GPa. Electronic degrees of freedom was computed using 350 eV plane-wave cut-off energy, 0.2 Å^{-1} gamma k-points spacing, and 0.2 eV Methfessel-Paxton smearing width. Electron exchange correlation functional was described by generalized gradient approximation and Perdew-Burke-Ernzerhof (GGA-PBE) parametrization.

Initial supercell configurations for AIMD were determined using Al-Sc binary phase diagram [66], and their compositions are marked with dotted lines in Figs. 1(a) and 1(b). We have examined 0.4 and 1 at.% Sc alloys for probing Sc-mediated liquid ordering and homogeneous nucleation. Simulations involving 0.4, and 1 at.% Sc were performed using cubic supercells containing 256 atoms [Figs. 2(a) and 2(b)]. They were constructed by randomly substituting *fcc*-Al lattice sites with Sc atoms. Pure Al (0 at.% Sc) was used as control [Fig. 2(c)]. We also constructed a 384 atom orthogonal simulation box containing an Al/Al_3Sc interface [Fig. 2(d)]. This allowed us to examine liquid ordering near the Al_3Sc intermetallic phase and its role on nucleating *fcc*-Al. Al_3Sc has a melting point of [Fig. 1(b)]. In the supercell shown in Fig. 2(d), *fcc*-Al and $L1_2$-Al_3Sc was constrained via cube-on-cube orientation relationship (OR), i.e., $\langle 001 \rangle_{FCC}$ // $\langle 001 \rangle_{Al_3Sc}$, because this OR was observed in the as-solidified microstructures of Al-Sc alloys [26,28]. All supercells were first annealed at 1450 K for 50 picoseconds (ps). Equilibration at 1450 K was achieved within ∼35 ps for both types of supercells. Subsequently, they were annealed at 950 K. Although, temperatures were carefully controlled in our simulations, we noted a variation of ±30–50 K from the
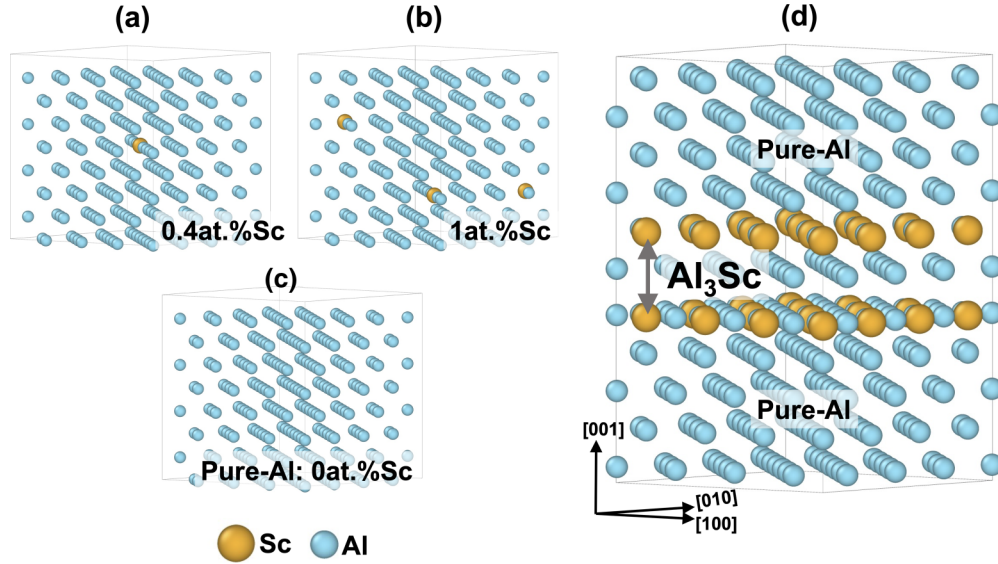
FIG. 2. Supercells used in the AIMD simulations. Simulation boxes with (a) 0.4 at.% Sc, (b) 1 at.% Sc and (c) 0 at.% Sc concentrations made of 256 atoms, and (c) fcc-Al/L1$_2$-Al$_3$Sc interfacial supercell comprising 384 atoms.

target value. Such variations will induce density fluctuations within liquid phase [67], and trigger nucleation events while annealing at 950 K. This subtle temperature-related effects allowed us to examine the potency of L1$_2$-Al$_3$S and Sc content on the nucleation.

Local atomic coordination in liquid environment was characterized using polyhedral template matching (PTM) algorithm [44,68–71] (also see Supplemental Material [72]). PTM identifies local atomic coordination based on well-known structures, e.g., fcc, bcc, hcp, and icosahedral. Our past studies on Al-Sm and Ni-Cr alloys have indicated that PTM is better suited for capturing structures within liquid phase compared to techniques like common neighbor analysis (CNA) algorithm [6,23,42]. PTM uses a metric called root mean squared deviation (RMSD), which quantifies the difference between an observed structure and a known coordination [44]. We found that RMSD = 0.15 optimally captured structures at 950 and 1450 K, while RMSD < 0.15 or RMSD > 0.15 yielded false positives. However, this feature also limited PTM's ability to detect in-liquid ordering when their local coordination substantially deviated from known structures. This matter was tackled by using techniques described in Sec. II B. Ovito was used for visualizing structures obtained from our simulations [73].

Ordering near Al-Al$_3$Sc interface was characterized by computing atomic density profiles $\rho(z)$ using [30,38,39,74–76],

$$\rho(z) = \frac{N_z(t)}{(L_x L_y \Delta z)}, \tag{1}$$

where L_x and L_y are the in-plane dimensions along x and y axes, respectively, and z axis was perpendicular to the interface or parallel to the longest dimension of the simulation box [see Fig. 2(d)]. $N_z(t)$ is the number of atoms sampled inside thin slices of volume $(L_x L_y \Delta z)$ at time t. Here, L_x and L_y depended on the simulation temperature, while $\Delta z = 0.15$ Å.

Finally, diffusive atomic movement was examined by computing the mean-squared displacement (MSD) of each species using the relationship [35,77]

$$\langle R_i^2(t) \rangle = \left\langle \sum_{j=1}^{N_i} |\vec{R}_j(t+t_0) - \vec{R}_j(t_0)|^2 \right\rangle, \tag{2}$$

where $\langle R_i^2(t) \rangle$ is the MSD of the ith component, N_i is the number of ith atoms in the simulation box, R_j is the position of jth atom in Cartesian coordinate frame of reference, and t_0 is the starting time.

B. Implementation of unsupervised learning techniques

To detect in-liquid structural ordering, three-dimensional (3D) atomic coordinates from AIMD snapshots were processed by sequentially applying *structural fingerprinting*, *dimensionality reduction* and *cluster analysis*. The next three paragraphs will describe each step.

Structural fingerprinting. We have used smooth overlap of atomic positions (SOAP) formalism to numerically encode local structures or atomic geometries present inside the AIMD supercells. SOAP formalism converts that 3D atomic Cartesian coordinates into a system that is invariant to translation, rotation, and permutation [78,79]. Specifically, SOAP uses Gaussian smoothing functions to perform a numerical expansion centered on atomic positions [78,79]. This approach captures local structural information by transforming 3D atomic coordinates ($\bar{r}_{ii}$) into higher dimension $N \times M$ space, where N and M are the number of supercell atoms and expansion terms, respectively. For our purposes, $M = 546$ was deemed sufficient to analyze AIMD results. This selection resulted in 139 776 and 209 664 data points for supercells containing 256 [Figs. 2(a)–2(d)] and 384 [Fig. 2(e)] atoms, respectively.

Dimensionality reduction. Analysis and visualization of data in $N \times M$ dimension presents some technical and
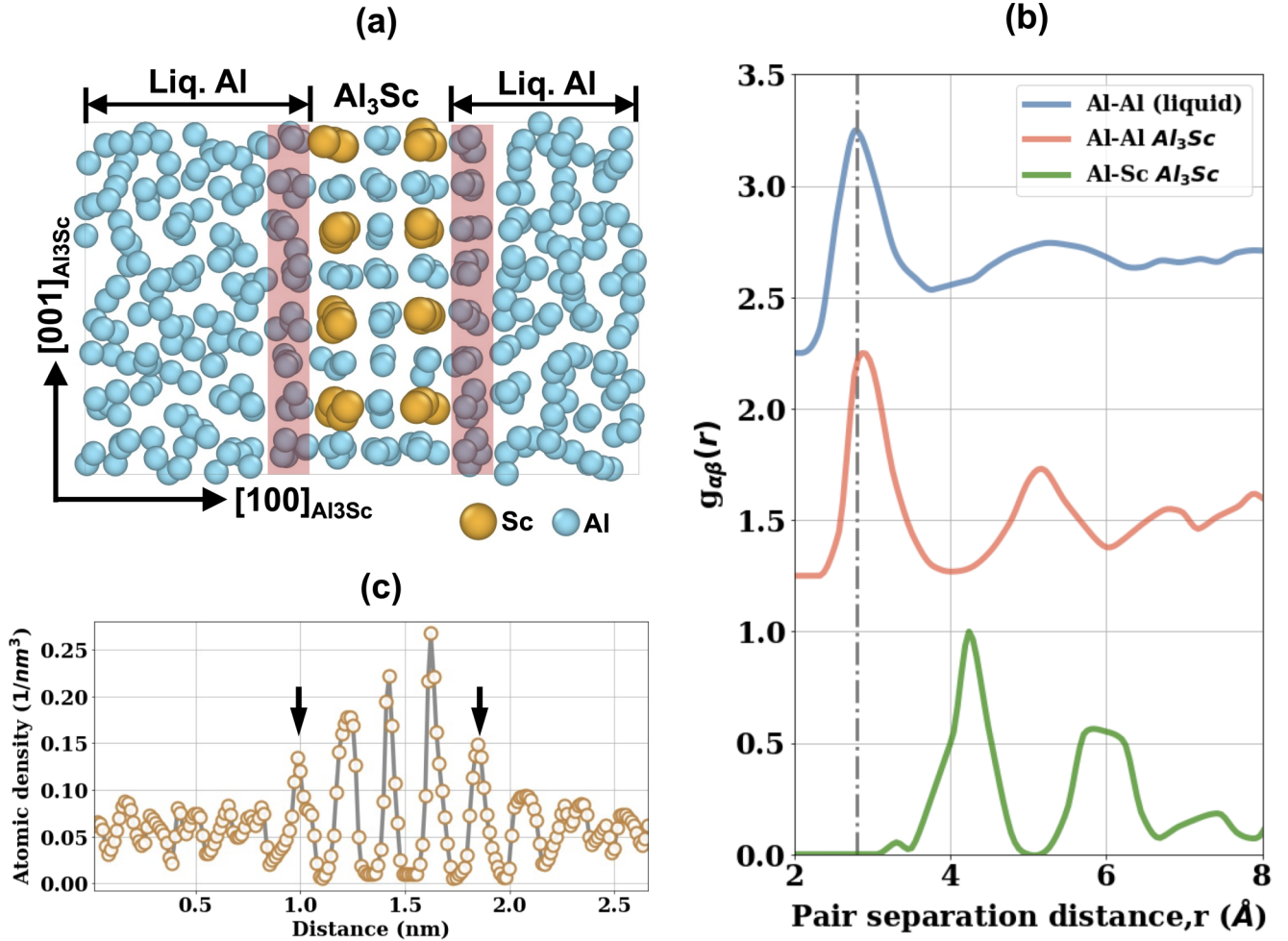
FIG. 3. AIMD of Al/L1$_2$-Al$_3$Sc interfacial supercell after 50 ps of annealing at 1450 K. (a) atomic configuration showing liquid-Al and crystalline Al$_3$Sc phases; (b) plots comparing partial radial distributions extracted from liquid-Al and crystalline Al$_3$Sc phases; and (c) atomic density profile across liquid-Al/L1$_2$-Al$_3$Sc interface. Ordered planes are indicated using shaded red colored boxes in panel (a) and arrows in (c).

practical hurdles. This limitation was circumvented by employing t-distributed stochastic neighbor embedding (t-SNE) to represent such higher dimensional data in 2D eigenspace [50]. t-SNE is shown to be better at preserving the local structure of data compared to techniques like principle component analysis, even after dimensional transformation [50]; meaning, t-SNE-based $N \times M$ to 2D transformation preserves structural fingerprints captured by SOAP. t-SNE is sensitive to the "perplexity" hyperparameter [50], which takes into account the number of nearest neighbors around a datum during dimensionality reduction. Extensive testing indicated that a perplexity value of 15 was best suited for our needs, which was consistently used for all analysis. Hereafter, the dimensionality reduced datasets will be referred as "t-SNE-based 2D reduced space".

Cluster analysis. Atoms within in-liquid ordered structures were detected by this approach. Atom-clusters that formed in-liquid ordered structures were detected by applying density-based spatial clustering of applications with noise (DBSCAN) algorithm to the t-SNE-based 2D reduced space. DBSCAN was chosen because it is capable of identifying clusters of arbitrary shapes along with outliers [56–60]. This

unsupervised algorithm primarily depends on two hyperparameters: (i) radius of a circle around datum in 2D space (ϵ) and (ii) the minimum number of points within ϵ forming a cluster (N_{min}) – $N_{min} = 6$ was found to reasonably detect clusters of varying sizes. Furthermore, hyperparameter ϵ influences the number of clusters yielded by DBSCAN [56], and an "optimum" value avoids detecting redundant clusters. Towards that end, we have employed K-nearest neighbor (KNN) algorithm to determine optimal ϵ [57,80,81].

We have used DScribe library to convert 3D Cartesian coordinates of atoms into SOAP-based invariant representation [82]. Scikit-learn was used to perform t-SNE-based dimensionality reduction, DBSCAN-based cluster analysis and KNN for finding optimum hyperparameters [83].

III. RESULTS

Our results are broadly divided in two parts. First, we present observations on ordering within liquid phase at 1450 K (Secs. III A and III B). Subsequently, we show how such ordering affect crystalline phase formation after annealing at a lower temperature of 950 K (Sec. III C), and the
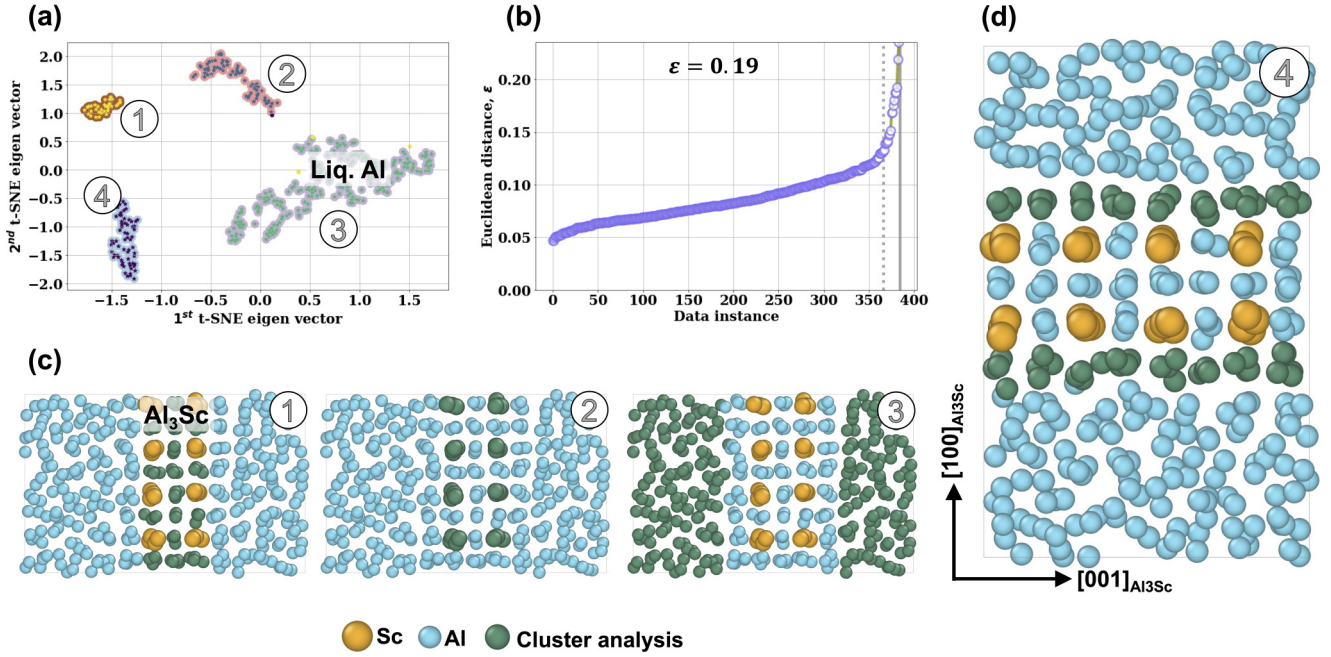
FIG. 4. Implementation of unsupervised learning techniques to liquid-Al/L1$_2$-Al$_3$Sc interfacial supercell that was annealed at 1450 K for 50 ps. (a) Scatter plot showing clusters detected by applying DBSCAN to t-SNE reduced space; (b) elbow plot used for selecting ϵ by applying KNN to t-SNE reduced space; (c) supercells showing atomic locations corresponding to cluster number 1, 2, and 3 in panel (a); and (d) interfacial ordered plane obtained from the 4th cluster in panel (a). Atoms corresponding to each cluster shown using green color in panels (c) and (d). In panel (b), ϵ corresponded to the intersection of solid line with KNN-curve.

combined movement Al and Sc atoms in the liquid phase (Sec. III D).

A. Al/L1$_2$-Al$_3$Sc interfacial ordering at 1450 K

We will first investigate ordering near Al-Al$_3$Sc interface, because several experimental studies have reported that L1$_2$-Al$_3$Sc phase assist in the heterogeneous nucleation of fcc-Al [26–29]. Therefore, it is necessary to understand the structural precursor preceding nucleation. Figure 3 shows an AIMD snapshot of an Al-Al$_3$Sc interface after 50 ps of annealing at 1450 K. Al$_3$Sc showed small deviations in positions of Al and Sc atoms from the crystalline lattice [compare Figs. 1(e) and 3(a)]. In contrast, Al atoms, that were outside of Al$_3$Sc, formed an amorphous structure; consistent with liquid phase. We have further examined both phases by comparing $g_{AlAl}(r)$, $g_{AlSc}(r)$, and $g_{ScSc}(r)$ partial radial distribution functions (PDFs) using Fig. 3(b) (see Supplemental Material [72]), and computing atomic density profiles across the Al/Al$_3$Sc interface [Fig. 3(c)]. The $g_{AlSc}(r)$ and $g_{ScSc}(r)$ PDFs in Fig. 3(b) showed distinct, periodic peaks corresponding to crystalline planes within Al$_3$Sc. PTM analysis also indicated that Al$_3$Sc have *fcc* coordination (discussed latter). It appears that thermal vibration at 1450 K was insufficient transform L1$_2$-Al$_3$Sc into liquid phase. However, $g_{AlAl}(r)$ extracted from the Al regions outside of Al$_3$Sc corresponded to an amorphous structure [6,35,77]. Thus, phases obtained from our AIMD simulations were consistent with the equilibrium Al-Sc phase diagram, i.e., crystalline Al$_3$Sc coexisting within liquid at 1450 K.

Figure 3(c) shows an atomic density profile across the liquid-Al/L1$_2$-Al$_3$Sc interface, which was computed using Eq. (1). This profile was obtained after averaging atomic positions over 1000 AIMD iterations or snapshots spanning 5 ps (each time step was 0.005 ps, see Sec. II A). Such atomic density profiles are typically used for identifying ordering near interfacial regions in the literature [30,38,39,74–76]. The key feature in Fig. 3(c) are three distinct peaks, whose maxima located within ∼1.25–1.75 nm and corresponded to (200) planes in L1$_2$-Al$_3$Sc [compare Figs. 3(a) and 3(c)]. Interestingly, two additional peaks were noted on either side of Al$_3$Sc at ∼1 and 1.87 nm; they are also indicated with arrows in Fig. 3(c). These peaks are distinct from the background, and indicate ordering within the adjacent liquid domain. The two peaks can be correlated to thin strips of Al atoms that are located at the interface of liquid-Al and L1$_2$-Al$_3$Sc in Fig. 3(a) (marked with shaded boxes). Thus, our AIMD simulations revealed the presence of ordering at liquid-Al/L1$_2$-Al$_3$Sc interface.

It should be emphasized that interfacial ordering could not be detected using PTM algorithm, since it could not correlate the crystallography of ordered layer with any known coordination (see Sec. II A). Therefore, we have employed unsupervised learning (UL) techniques based on local structure fingerprinting using SOAP, t-SNE-based dimensionality reduction, and cluster analysis using DBSCAN (see Sec. II B). It is also worth mentioning that a successful application of these techniques must yield results that are consistent with those obtained from "conventional" approaches, i.e., Figs. 3(a) and 3(c). In other words, the UL approach must identify interfacial ordering of Al atoms, structural features within Al$_3$Sc, and, broadly, distinguish between solid and liquid phase. Keeping these factors in mind, next we present results obtained from UL analysis of AIMD snapshots.
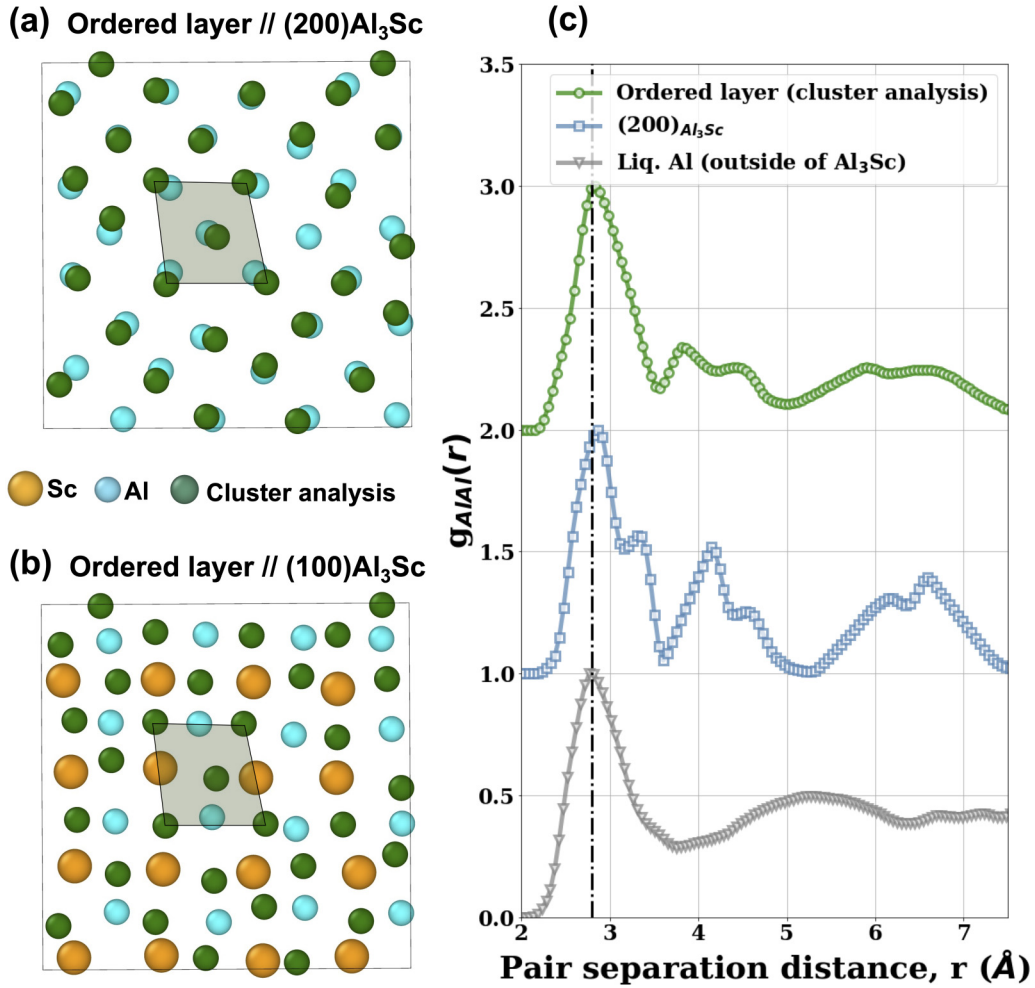
FIG. 5. Geometry of interfacial ordered layers and their comparison with Al$_3$Sc crystallographic planes. $(100)_{fcc-\text{Al}}$ overlaid on (a) (200) and (b) (100) planes of L1$_2$-Al$_3$Sc, and (c) plots comparing Al-Al partial radial distributions extracted from $(100)_{fcc-\text{Al}}$, $(200)_{Al_3Sc}$ and liquid-Al. Atoms belonging to the interfacial layer are shown using green color in panels (a) and (b).

1. Unsupervised learning-based detection of Al/Al$_3$Sc interfacial ordering

Figure 4(a) shows a scatter plot of t-SNE-based 2D reduced space corresponding to liquid-Al/L1$_2$-Al$_3$Sc interface, which was obtained after annealing at 1450 K for 50 ps. (This plot is a 2D eigenspace representation of data residing in a multidimensional space, see Sec. II B). Four clusters are identified using DBSCAN, and they are indicated using different colors. These clusters were obtained using hyperparameter $\epsilon = 0.19$ that was determined from the plot shown Fig. 4(b). This "elbow" plot was determined using KNN algorithm, which allowed us to compute nearest-neighbor distances between points, or data instances, in the t-SNE-based 2D reduced space. Typically, ϵ is extracted from the "knee" of an elbow plot [57,80,81,84,85], which is indicated with a dotted line in Fig. 4(b). However, this method subdivided the amorphous liquid phase into redundant clusters (see Fig. S1 within the Supplemental Material [72]); meaning, it incorrectly attributed structure to a random distribution of atoms. We found that ϵ determined from tangent to the asymptotic portion of the plot yielded physically reasonable clusters

[bold line in Fig. 4(b)]. We have employed this latter approach of analysis throughout the paper.

Next, we extracted atomic positions corresponding to the four clusters shown in Fig. 4(a). Towards that end, Figs. 4(c) and 4(d) depict atoms corresponding to each cluster within the interfacial supercell. (Atoms belonging to a cluster are colored green.) Our analyses show that cluster #1 and #2 denote Al and Sc atoms within L1$_2$-Al$_3$Sc, respectively, while #3 correlates to the liquid-Al phase [Fig. 4(c)]. Figure 4(d) shows that our UL approach has successfully identified Al atoms belonging to the ordered layer near the interface, i.e., via cluster #4. Thus, our choice of UL parameters could correctly identify L1$_2$-Al$_3$Sc structural features, and, broadly separate solid and liquid phases-consistent with results obtained using techniques employed in Sec. III A.

Figures 5(a) and 5(b) shows the atomic arrangement within the ordered cluster against the backdrop of $(200)_{Al_3Sc}$ (containing only Al atoms) and $(100)_{Al_3Sc}$ (containing Al and Sc atoms) planes, respectively. We find that atomic arrangement within the ordered layer resembled that of $(200)_{Al_3Sc}$, although it is physically closer to $(100)_{Al_3Sc}$ [see Fig. 4(d)]. A careful
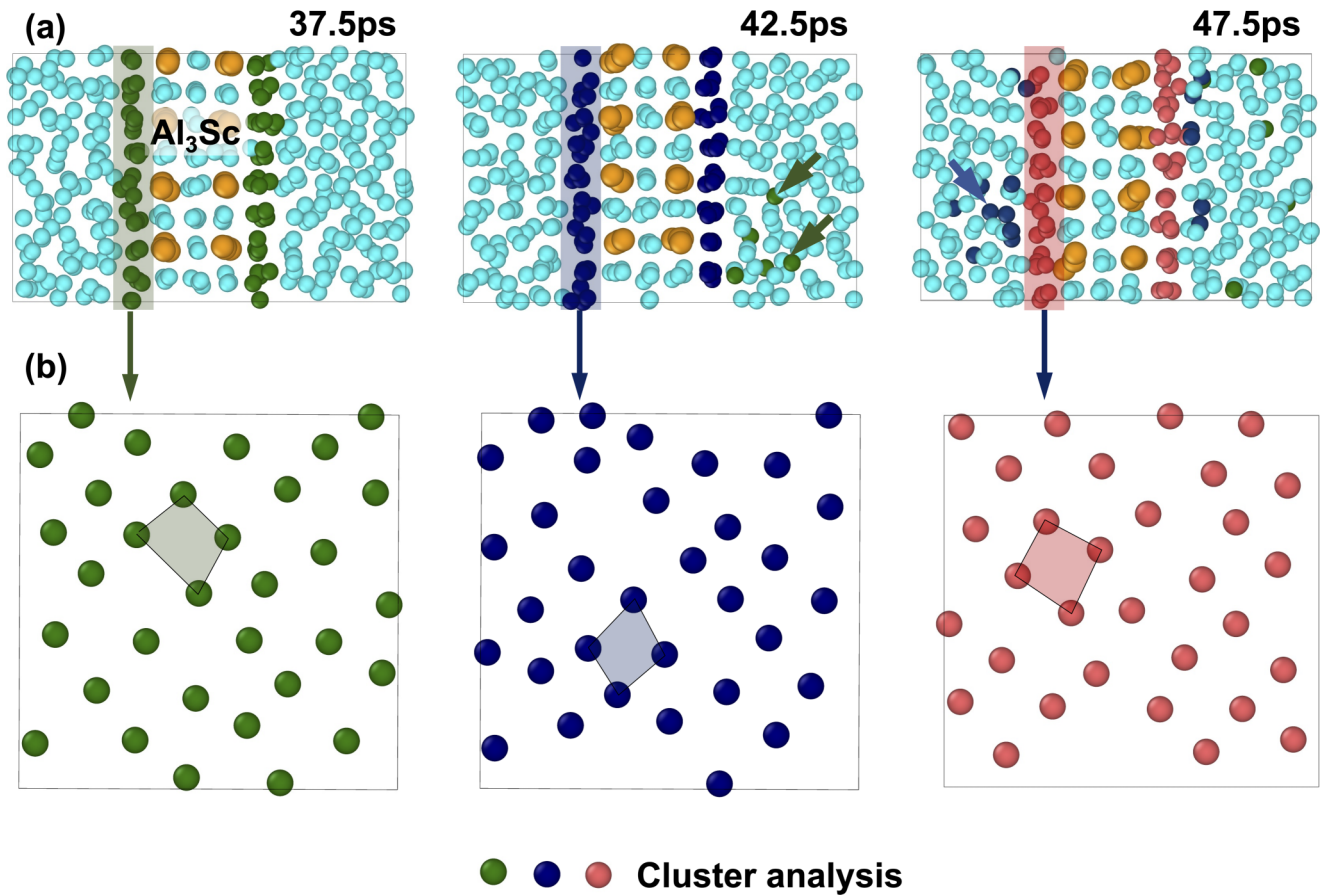
FIG. 6.   AIMD snapshots showing (a) atomic within the simulation volume, and (b) geometric integrity of interfacial ordered layers after 37.5, 42.5, and 47.5 ps of annealing at 1450 K. Atoms belonging to the ordered layers from previous time steps are indicated using arrows in (a). Geometric integrity within the ordered layer is schematically shown by the persistence of distorted square motifs in all the three time steps.

inspection of atomic arrangement within the ordered layer indicated that it comprised of in-plane "distorted" square motifs, and these motifs were comparable to face-centered planes of *fcc* structure [schematically shown in Fig. 5(a) and 5(b)]. We have further compared and contrasted the structure of ordered layer with $(200)_{Al_3Sc}$ and liquid-Al by comparing their $g_{AlAl}(r)$ PDFs [Fig. 5(c)]. Ordering did not change the location of the peak corresponding to the 1st nearest-neighbor (NN) coordination shell. In all the three cases, this 1st NN peak was located at ~ 2.8 Å (dotted line in Fig. 5(c)]. In contrast, ordering introduced a significant difference in the "structure" and location of the 2nd NN peak compared to liquid-Al. This was manifested as a doublet, which was located between ~ 3.8 and 4.5 Å. Such a "doublet" structure was also noted in the 2nd NN of $(200)_{Al_3Sc}$ PDF, which indicated that the ordered layer is structurally comparable to $(200)_{Al_3Sc}$. Broadly, these results show that intermetallic Al$_3$Sc can alter its immediate liquid environment, i.e., within few angstroms, to produce structural/crystallographic correspondence with itself. Further discussion regarding this matter will be delayed till Sec. IV.

We conclude this section by qualitatively examining the influence of interfacial ordered layer (near Al$_3$Sc) on the transport properties of Al atoms. This transport dynamics is elucidated in Fig. 6 using two views: cross sectional view of the supercell [Fig. 6(a)]; and perpendicular view of an ordered

layer [Fig. 6(b)]. In these views, different colors were used to denote interfacial atoms at each snapshot, i.e., 37.5 (green), 42.5(blue), and 47.5 ps (red). (UL was used to detect atoms within the ordered layer.) We find that the interfacial atoms were not perennially trapped within the order layer (see red and blue atoms), and they can diffuse into the adjoining liquid domain [marked with arrows in Fig. 6(a)]. Interestingly, such atomic movement did not alter the overall structure in that layer. Persistence of that interfacial structure was corroborated by the presence in-plane "distorted" square motifs in the three snapshots indicated in Fig. 6(b). Thus, the ordered layer was geometrically persistent, but constitutionally transient.

B. Sc-mediated in-liquid ordering at 1450 K

We have also examined ordering within the liquid phase of 0.4 and 1.0 at.% Sc alloys, which were annealed at 1450 K for 50 ps (see Sec. II A). Results were compared with pure Al or 0 at.% Sc. Figure 7(a) show snapshots at 50 ps, including pure Al, while Fig. 7(b) compares and contrasts their corresponding g_{AlAl} PDFs. They showed that Sc concentration did not change the location of the 1st nearest neighbor (NN) peak, but discernible differences were noted around the broad 2nd NN peaks of 0.4 and 1.0 at.% Sc, when compared with pure Al. These differences manifested in two ways [Fig. 7(b)]: (i) location of the 2nd NN was marginally shifted to the right
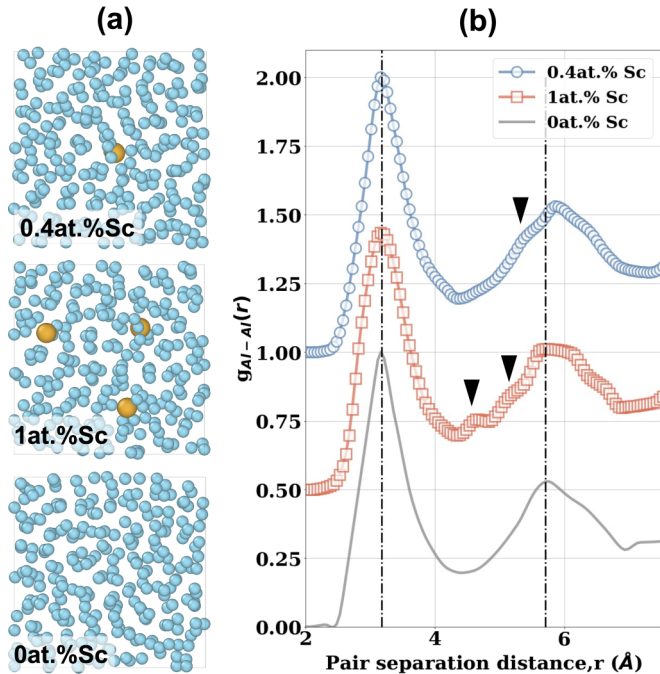
(a)

(b)

FIG. 7. AIMD of supercells containing 0, 0.4, and 1 at.% Sc after 50 ps of annealing at 1450 K. (a) snapshots showing atomic configuration in three supercells, and (b) plots comparing their Al-Al partial radial distribution functions. Peaks due to in-liquid ordering in 0.4 and 1 at.% Sc are indicated using arrows.

compared to 0 at.% Sc (see dotted the line near ~5.7 Å); and (ii) development of shoulders between ~5−5.7 Å (marked with arrows), which were not observed in case of 0 at.% Sc. (An additional peak was noted at ~4.6 Å in case of 1 at.% Sc.) These observations suggested the presence of an in-liquid structure in the alloys, and such structures seemed to affect second nearest neighbor atomic arrangement. Next, we have employed UL-based techniques to better understand these in-liquid structures at 1450 K.

1. Unsupervised learning-based detection of Sc-mediated in-liquid ordering

Figures 8(a1) and 8(b1) show scatter plots of t-SNE-based 2D reduced space obtained from the invariant representation of 0.4, and 1.0 at.% Sc datasets, respectively. In these plots, clusters were identified by employing techniques that were similar to those used for analyzing interfacial supercells (see Sec. III A 1). In a few cases, we note that DBSCAN-based cluster analysis could not group data points into clusters, and these "anomalies" are indicated with an "x" in the plots, e.g., see datum marked with an arrow in Fig. 8(a1). Notwithstanding, the smaller clusters in Figs. 8(a1) and 8(b1) indicated the presence of in-liquid structures, while the largest cluster corresponded to liquid phase (light-blue color). In comparison, cluster analysis of pure Al revealed liquid phase, only. This matter is illustrated in Fig. 9 that shows t-SNE-based 2D reduced space analysis of 0 at.% Sc or pure Al at three time snapshots, i.e., 30, 40, and 50 ps. Here, DBSCAN detected one large cluster in each time step, which indicated absence of in-liquid ordering; unlike 0.4, and 1.0 at.% Sc dataset. Next,

we turn our attention to the structures revealed by the UL within liquid phase of 0.4 and 1.0 at.% Sc that were annealed at 1450 K for 50 ps. Their structures are shown in Figs. 8(a2) and 8(b2), and they corresponded to clusters marked with ovals in Figs. 8(a1) and 8(b1).

Figure 8(a2) shows that 0.4 at.% Sc contained a Sc-centered polyhedron, where the cage-like outer shell was comprised of Al atoms. This structure did not resemble well-known symmetries, e.g., *fcc* (space group $Fm\bar{3}m$), *bcc* (space group $Im\bar{3}m$), or *hcp* (space group $P6_3mmc$), due to which it avoided detection from PTM algorithm. However, one viewing axis revealed that it had a "distorted", yet recognizable, fivefold symmetry, which is schematically shown with a red colored line in Fig. 8(a2). This indicated that cage-like structure contained symmetry elements resembling a "highly distorted" icosahedron. In case of 1 at.% Sc [Fig. 8(b2)], 50 ps of annealing resulted in interconnected cages, where each cage is centered on a Sc atom. It must be pointed out that cluster analysis of 1 at.% Sc yielded the outer Al-based interconnected cages. Detailed examination of the local environment around those cages revealed their correlation with Sc atoms. Additionally, cluster analysis of 1 at.% Sc indicated another small cluster [marked with an arrow in Fig. 8(b1)], which corresponded to Al atoms in triangular and linear arrangements [inset in Fig. 8(b1)]. The significance of such simple geometries is currently unclear; it is likely a transient structure that dissolves back into the liquid. Regardless, these results show key structural elements in liquid Al-Sc alloys: (a) individual Sc atoms have a tendency to order liquid Al atoms around themselves; and (b) proximal Sc atoms will form interconnected 3D polyhedrons that share symmetry elements with an individual Sc-centered polyhedron.

We have further characterized these structures by extracting their respective g_{AlAl} PDFs from 0.4 and 1 at.% Sc, which are plotted in Fig. 8(c). Both individual and interconnected cages in 0.4 and 1.0 at.% Sc, respectively, showed multiple peaks due to ordering. Comparison with the "global" g_{AlAl} PDFs in Fig. 7(b) show that most of the peaks within ~2.5–4 Å pair separation distance are subsumed by the amorphous liquid background. However, signature of such structures in the global PDF are manifested near 2nd NN [of Fig. 7(b)] via the peaks centered around ~5 Å in Fig. 8(c); compare shaded area in Fig. 8(c) with Fig. 7(b).

We note that the ordered structures in 0.4 and 1 at.% Sc are geometrically different from liquid-Al/L1$_2$-Al$_3$Sc interface, i.e., polyhedral configurations vs distorted squares forming an ordered plane, respectively; compare Figs. 6 and 8(a2) and 8(b2). The ordered layer in the latter was physically trapped at the liquid-Al/L1$_2$-Al$_3$Sc interface, even though it exchanged Al atoms with its surrounding while annealing at 1450 K (Fig. 6). In comparison, annealing 0.4 and 1 at.% Sc at 1450 K influenced the shape evolution of individual cages/polyhedrons and their relative arrangements with the melt. In case of 0.4 at.% Sc, we found that a cage-like polyhedral structure with a recognizable fivefold symmetry emerges after ~45 ps [Fig. 10(a) and Fig. S2 within the Supplemental Material [72]), and persists till the duration of our simulations, i.e., 50 ps [see Sec. II A and Fig. 8(a2)]. It may be noted that, although AIMD simulations are limited to short temporal scales, our results suggested that
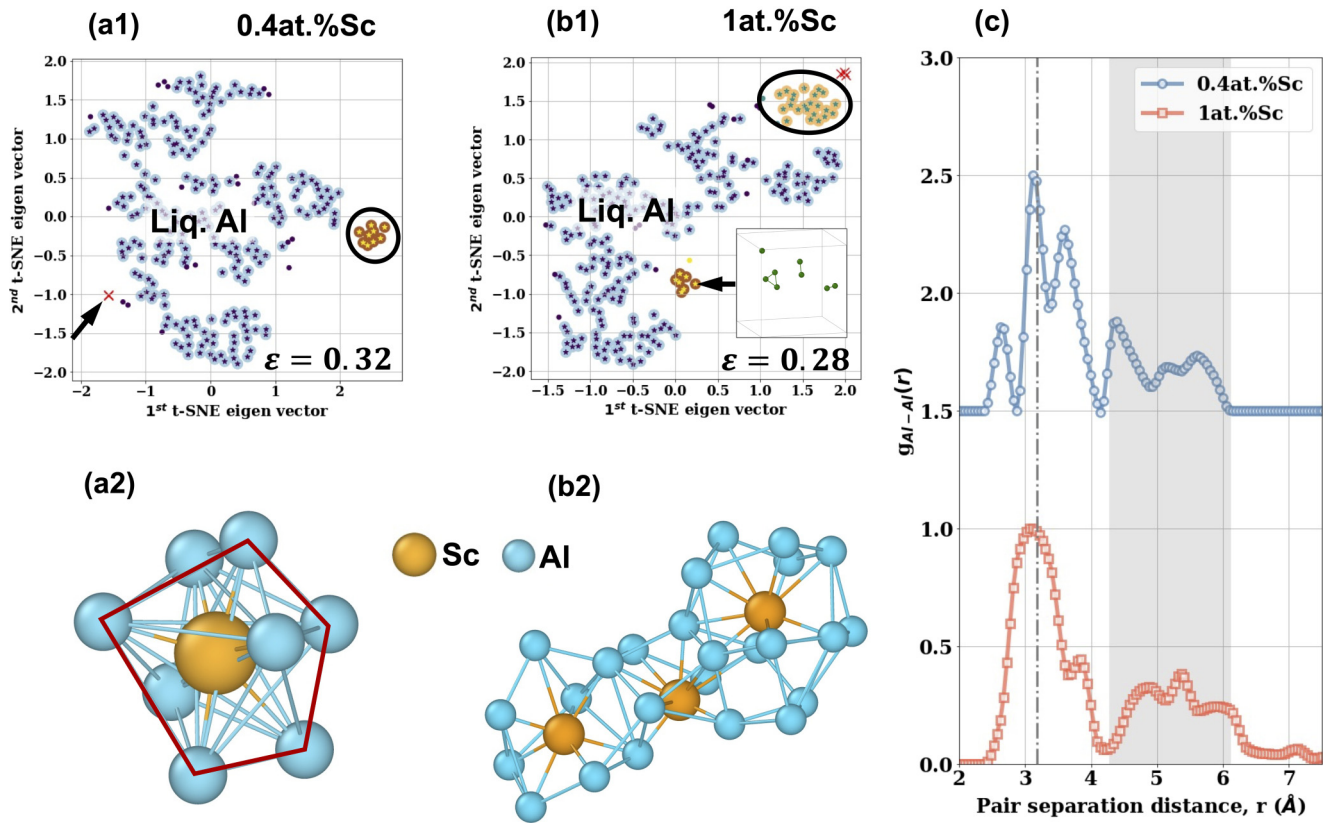
FIG. 8. Implementation of unsupervised learning techniques to 0.4 and 1 at.% Sc that were annealed at 1450 K for 50 ps. Scatter plots in (a1) and (b1) identify clusters due to in-liquid ordering in 0.4 and 1 at.% Sc, respectively. Clusters corresponding to in-liquid ordering are shown using ovals in panels (a1) and (b1). 0.4 at.% Sc contained (a2) a cage-like polyhedral structure resembling a distorted icosahedron, while 1 at.% Sc comprised of (b2) interconnected cage-like of polyhedrons. Inset in panel (b2) shows the structure corresponding to the smaller cluster in 1 at.% Sc. (c) plots comparing Al-Al partial radial distribution function extracted from individual polyhedron and interconnected structures.

such distorted icosahedral structures will persist for longer, experimentally observable duration, consistent with literature [14]. (These distorted icosahedrons were also observed at 950 K, see Sec. III C 2.)

Furthermore, such polyhedron shape evolution was associated with their movement in the liquid that commensurated with Sc diffusion. We depict their movement in Fig. 10(b) using 1 at.% Sc, which shows the configurational evolution of three Sc-centered cages at 37.5 and 50 ps. Figure 10

shows the existence of individual cages when Sc atoms are far apart (37.5 ps). But the proximally located Sc atoms, due to their diffusive movement, allowed the cages to form an interconnected structure at 50 ps. It is important to note that the same group of Al atoms do not always move with Sc atoms. Instead, Sc dynamically collected Al atoms from its surrounding to form a transient, enveloping cage. Thus, Sc-centered polyhedral cage-like structure were geometrically persistent but constitutionally
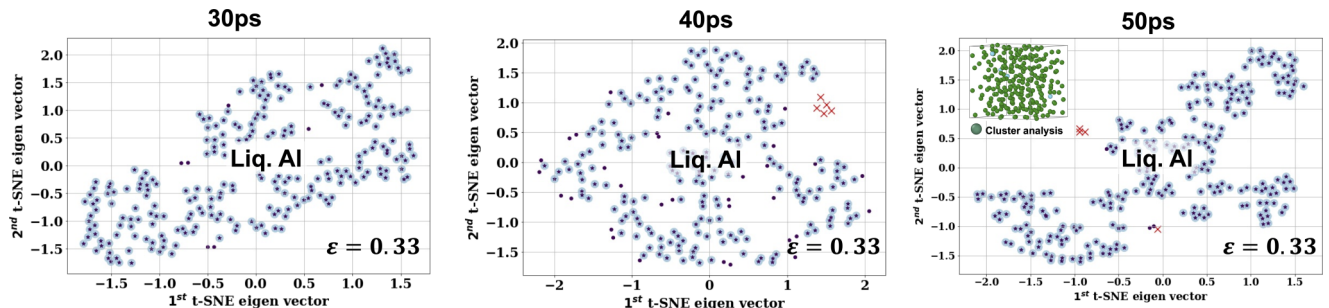

FIG. 9. Implementation of unsupervised learning techniques to 0 at.% Sc or pure Al that was annealed at 1450 K for 30, 40, and 50 ps. The inset corresponding to 50 ps shows the structure obtained from DBSCAN-based cluster analysis.

(a) 0.4at.%Sc

40ps   45ps   47ps

Sc   Al

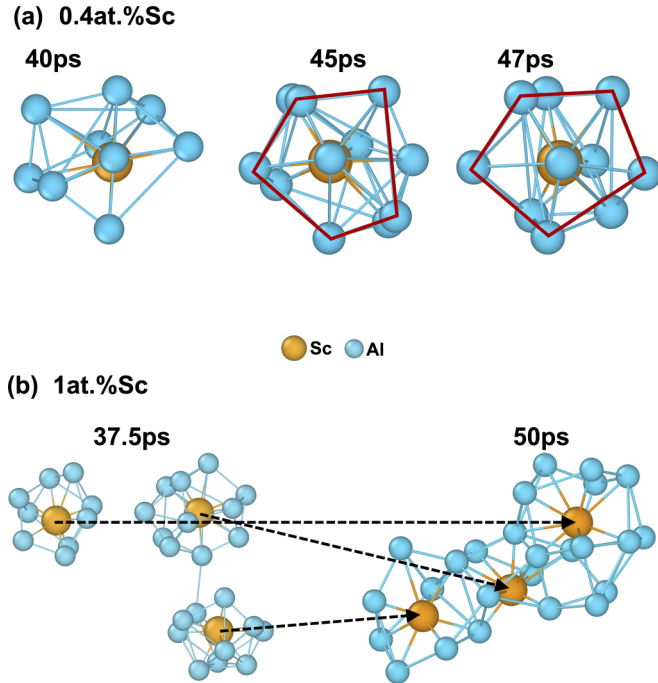**(b) 1at.%Sc**

37.5ps   50ps

FIG. 10. Structural changes during annealing at 1450 K: (a) shape evolution of Sc-centered cage-like structures in 0.4 at.% Sc, where the recognizable fivefold symmetry in shown with red lines; and (b) configuration evolution of Sc-centered cage-like polyhedron in 1 at.% Sc. Dotted arrows in panel (b) maps Sc positions between two snapshots.

transient—comparable to liquid-Al/Al$_3$Sc interfacial ordering at 1450 K. Influence of these Sc-centered cages on the diffusive movement of Al and Sc will be presented in Sec. III D.

C. Effect of in-liquid ordering on crystallization

The 0.4 and 1 at.% Sc alloys, and liquid-Al/L1$_2$-Al$_3$Sc interfacial supercells were subsequently annealed at 950 K to examine the influence of in-liquid ordering on nucleation. Before presenting our results, we will emphasize two vital aspects regrading these simulations. First, due to the small time scales involved, i.e., picoseconds (10^{-12} s), AIMD simulations are capable of probing transient and metastable structure. Therefore, AIMD can determine the structures of metastable precritical nucleus and correlate it with in-liquid ordering, e.g., see Fig. 10. However, such small time scales may not permit us to capture the transformation of metastable precritical nuclei into the equilibrium structure/phase in many cases. Classical MD simulations are better suited for such cases, because they examine events over relatively longer time scales, i.e., nanoseconds (10^{-9} s) [16,23,35,77,86], which is beyond the scope of the current study. (In Sec. IV B, we will discuss how AIMD results can be extended using experimental observations to gain valuable insights). Second, in several alloys, the structure of metastable pre-critical nuclei are *fcc*, *bcc*, *hcp*, or combinations thereof [16–18,20–23,67,86–90], and these well-known structures could be easily detected using conventional PTM algorithm (Sec. II A) [6,23]. Therefore, we have employed PTM to independently evaluate structural
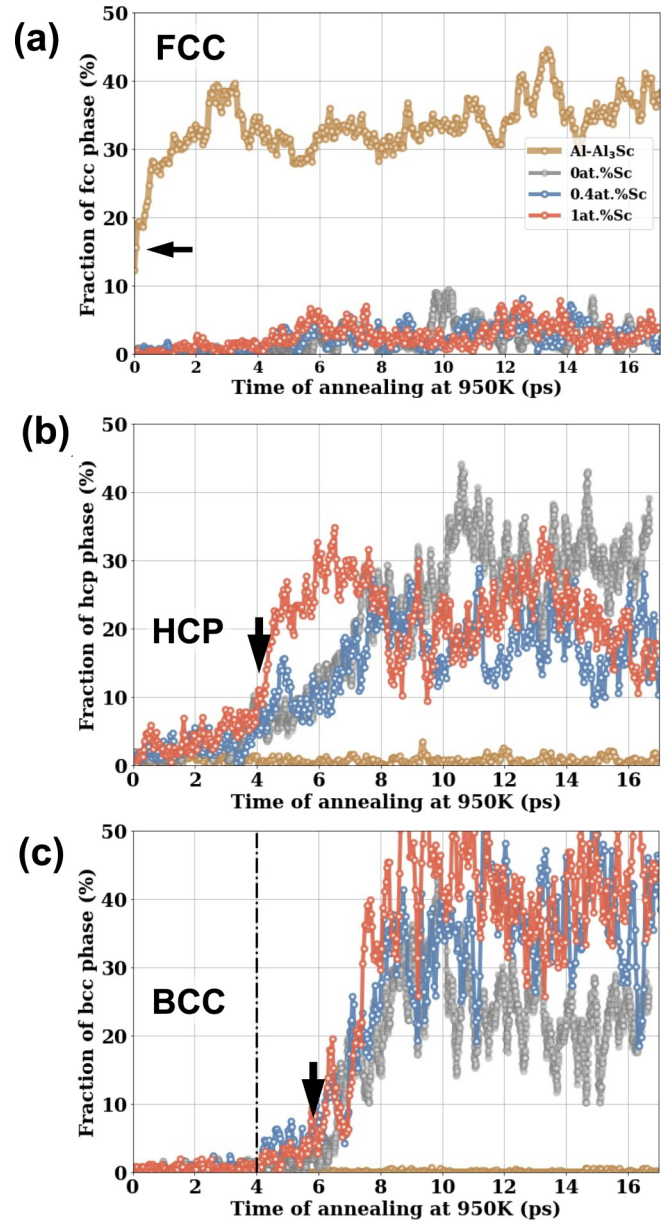

FIG. 11. Quantification of phase fractions during annealing at 950 K. Phase fraction vs time plots compare evolution of (a) *fcc*, (b) *bcc*, and (c) *hcp* structures within liquid-Al/L1$_2$-Al$_3$Sc, 0 at.% Sc, 0.4 at.% Sc, and 1 at.% Sc supercells.

changes during crystallization (discussed next using Fig. 11 and Table I), and coupled such quantitative assessment with UL-based techniques, i.e., DBSCAN-based cluster analysis of t-SNE-based 2D reduced space, to examine in-liquid ordering mediated nucleation (Secs. III C 1 and III C 2).

Plots in Fig. 11 show the relative fractions of *fcc*, *bcc*, and *hcp* coordinated structures in liquid-Al/L1$_2$-Al$_3$Sc, 0.4 and 1 at.% Sc alloys, and pure Al (0 at.% Sc) as a function of annealing time. AIMD simulations at 950 K was performed till 20 ps, and key structural changes were captured within 16 ps of annealing. We have also extracted phase average fractions from the plots in Fig. 11, and listed them in Table I.

Figure 11(a) shows that *fcc* formed in substantially higher average fraction, i.e., ∼35%, in liquid-Al/L1$_2$-Al$_3$Sc within

TABLE I. Average phase fractions of fcc, hcp, bcc in pure Al, 0.4 at.% Sc, 1 at.% Sc, and Al/L1$_2$-Al$_3$Sc. Statistics was determined by extracting data within 10–16 ps of annealing. Influence of ordering on phase fractions are indicated using blue colored fonts.

System	fcc	hcp	bcc
Al/L1$_2$-Al$_3$Sc	**35.7 ± 3.3**	0.7 ± 0.6[a]	0.1 ± 0.17[a]
0.3 at.% Sc	3.3 ± 1.4[a]	17.4 ± 4.0	**37.8 ± 7.0**
1.0 at.% Sc	3.3 ± 1.8[a]	22.6 ± 4.0	**40.4 ± 5.8**
0 at.% Sc (pure Al)	3.1 ± 1.7[a]	30.4 ± 5.0	23.1 ± 5.5

[a]negligible presence.

$\sim$1 ps, while others had a substantially lower fcc fraction, i.e., $< \sim 10\%$. It should be pointed out that, prior to annealing, liquid-Al/L1$_2$-Al$_3$Sc contained an fcc ordered Al$_3$Sc phase, which corresponded to $\sim$15% fcc fraction [indicated with an arrow in Fig. 11(a)]. Therefore, annealing at 950 K caused an additional $\sim$20% increase in the fcc fraction. This corresponded to the amount of amorphous liquid phase that was converted into fcc structure. Notwithstanding, these results suggested that the distorted square motifs (Fig. 6) within the ordered region of liquid-Al/L1$_2$-Al$_3$Sc favor the formation of fcc phase. Thus, the ordered layer next to L1$_2$-Al$_3$Sc promotes heterogeneous nucleation of the equilibrium fcc-Al phase (see Al-Sc phase diagram in Fig. 1).

In stark contrast, Figs. 11(b) and 11(c) show that metastable hcp and bcc structures dominated 0, 0.4, and 1 at.% Sc alloy rather than equilibrium fcc. All three systems shared several commonalities. They manifested an incubation time of prior to the formation of such well-defined metastable crystalline structures. During that incubation period, the cage-like structures in 0.4 and 1 at.% Sc alloy coexisted with amorphous liquid. Subsequently, hcp formed first after of annealing, and bcc formed latter at $\sim$6 ps. This $\sim$2 ps difference in the "appearance" times of the two structures suggested that hcp may facilitated the formation of bcc in all three cases.

However, there were two key differences between pure Al, and 0.4 and 1 at.% Sc. First, after $\sim$8 ps, these alloys had lower hcp [$\sim$20%, see Fig. 11(b)] but higher bcc [$\sim$40%, see Fig. 11(b)] average fractions compared to pure Al ($fcc \sim$30% and $bcc \sim$20%). These results imply that in-liquid cage-like structures in 0.4 and 1 at.% Sc biases the system towards higher bcc content compared to pure Al. Second, Fig. 11(b) shows that 1 at.% Sc experienced a rapid increase in hcp fraction at $\sim$4 ps, but it increased at a relatively gradual rate in case of 0 and 0.4% Sc. Furthermore, between $\sim$4–8 ps of annealing, 1 at.% Sc had a higher hcp fraction compared to 0 and 0.4% Sc between $\sim$4–8 ps of annealing. (hcp fraction in pure Al became more than 0.4 and 1 at.% Sc only after 8 ps). These observations suggested that number of cages, and possibly their arrangements [Figs. 8(a2)–8(b2) and Fig. 10], may affect hcp formation within liquid phase. Taken together, our AIMD simulations show that Sc-centered cages influence the sequence of structural changes during the nucleation of metastable structures within liquid Al.

To better understand the influence of in-liquid ordering, we have investigated in greater detail the structural changes near Al$_3$Sc (Sec. III C 1), and the relationship between Sc-centered cages and metastable structures (Sec. III C 2).

1. Al-Al$_3$Sc interface mediated heteroepitaxial nucleation

Figure 12 depicts the evolution of liquid-Al/L1$_2$-Al$_3$Sc interfacial structure via AIMD snapshots recorded immediately after 50 ps of annealing at 1450 K (0 ps), 9, and 12.5 ps. The local structure in each snapshot was determined using cluster analysis [Fig. 12(a)], PTM [Fig. 12(b)], and by computing atomic density profiles using Eq. (1) [Fig. 12(c)]. Both PTM and cluster analysis detected fcc coordinated atoms, while cluster analysis and atomic density profiles additionally identified non-fcc coordinated ordered layers. These extra layers are indicated with red colored arrows in Figs. 12(a)–12(c). In the snapshots recorded at 9 and 12.5 ps, those non-fcc coordinated ordered layers were located at liquid-Al/fcc-Al interface instead of liquid-Al/L1$_2$-Al$_3$Sc (e.g., at 0 ps). The atomic arrangement of such an ordered layer was similar to that observed at 1450 K (Fig. 6), i.e., they comprised of distorted square motifs. In essence, they represented ordering within liquid phase.

Furthermore, AIMD snapshots indicated that the proximity of such layers to the fcc coordinated regions caused a "cascading" sequence of events. The order layer at 0 ps facilitated the formation of $(100)_{fcc}$ after 9 ps. Upon further annealing, i.e., after 12.5 ps, the prior $(100)_{fcc}$ introduced ordering in the adjacent liquid. This process repeated itself during annealing at 950 K, till $\sim$20% of liquid Al is converted into equilibrium fcc-Al [see Sec. III C and Fig. 11(a)]. These results demonstrated that L1$_2$-Al$_3$Sc phase facilitates equilibrium fcc-Al formation via layer-by-layer or heteroepitaxial "deposition" of $(100)_{fcc}$ over $(100)_{Al_3Sc}$ planes.

2. Sc mediated homogeneous nucleation

The plots in Figs. 11(b) and 11(c) suggested that Sc-centered cages facilitated the formation of metastable hcp- and bcc-Al phases rather than equilibrium fcc-Al. Here, we examine their evolution within 0.4 and 1 at.% Sc using Figs. 13(a) and 13(b), respectively, to better understand the formation mechanism of metastable phases. Both alloys were also compared with pure Al results [Fig. 13(c)]. For all three cases, Fig. 13 show AIMD snapshots at the onset of hcp formation (4.25 ps) and when substantially amount of hcp and bcc crystallinity was achieved (10 ps). The evolving structures were examined by combining PTM for identifying hcp (red), bcc (blue), and fcc (green) coordinated atoms, and cluster analysis for detecting cage structures. In Figs. 13(a) and 13(b), atoms comprising Sc-centered cages are colored green and their location is schematically indicated using ellipses.

At 4.25 ps, the hcp coordinated Al atoms are segregated near the cages for 0.4 and 1 at.% Sc [indicated with arrows in Figs. 13(b) and 13(c)], while they were dispersed throughout the simulation volume of pure Al. Taken together, these results show the tendency of undercooled liquid Al to initially form hcp coordinated precritical nuclei. Sc-centered cages facilitates such nucleation by localizing them around their immediate neighborhood, and the extent of hcp formation appears to be guided by the number of cages and their mutual arrangement. For example, 1 at.% Sc contains relatively more hcp coordinated atoms than 0.4 at.% [Fig. 12(b)]. In the former, hcp atoms are located between two interconnected and lone polyhedrons, while the latter contained a single cage.
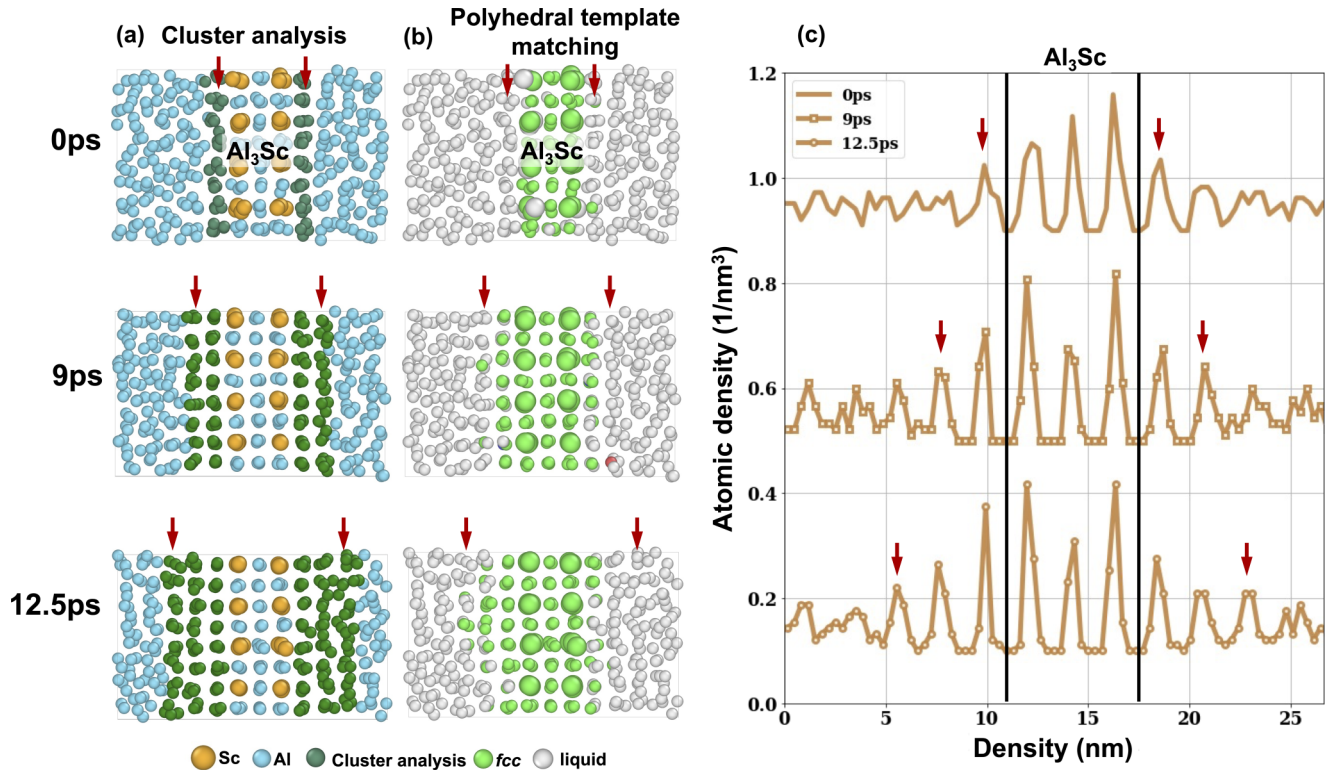
FIG. 12. $\{100\}_{fcc-Al}$ interfacial ordering mediated heteroepitaxial nucleation of equilibrium fcc at 950 K. AIMD snapshots showing the growth of fcc structure into the liquid phase via (a) cluster analysis, (b) polyhedra template matching, and (c) atomic density profiles at 0, 9, and 12.5 ps.

Therefore, it is likely such proximal arrangement of cages in 1 at.% Sc caused a rapid increase in hcp fraction seen in Fig. 10(b).

Transient bcc coordinated atoms were also noted near the hcp atoms at 4.25 ps. However, the formation of bcc structure within liquid phase is better understood by comparing and contrasting snapshots recorded at 10 ps. In case of pure Al, bcc coordinated structure was connected to a hcp region, which suggested that the latter facilitates bcc formation in pure Al [Fig. 13(c)]. Figures 13(a) and 13(b), corresponding to 0.4 and 1 at% Sc, respectively, showed that Sc-centered cages are intimately connected to hcp and, a relatively larger, bcc domains. This crucial observation demonstrates that those polyhedral cages act as *in situ* inoculants that, in conjunction with the evolving hcp domain (also see Fig. S3 within the Supplemental Material [72]), facilitate "heterogeneous" crystallization of bcc structure. Consequently, a higher fraction of bcc structure is noted in 0.4 and 1 at.% Sc compared to pure Al [Fig. 11(c)].

D. Effect of Sc-centered polyhedrons on the transport properties of Al and Sc

We have also quantified the effect of cage-like structures and crystallization on the diffusive movement of Al and Sc at 1450 and 950 K, respectively. For this purpose, MSD vs t^2 plots were computed using Eq. (2) for each temperature (Fig. 14). A linear MSD vs t^2 relationship corresponds to random atomic motion or Brownian movement [77,91], while

deviations from linearity is indicative of strong interatomic correlations that prevent random motion [36,37,77].

The linear plots in Fig. 14(a) showed that Al atoms experienced Brownian motion at 1450 K in 0, 0.4 and 1 at.% Sc. (We have used AIMD simulations between 40 and 50 ps to correlate atomic movement with in-liquid ordering at 1450 K.) This linear relationship allowed us to compute Al diffusion coefficients D_{Al} using the well-known Einstein's relationship [35,77],

$$D_{Al} = \lim_{t \to \infty} \frac{MSD}{6t}, \quad (3)$$

where MSD was computed using Eq. (2), and t is time. D_{Al} in 0, 0.4 and 1 at.% Sc were $1.54 \pm 0.28 \times 10^{-7}$, $1.82 \pm 0.37 \times 10^{-7}$, and $1.87 \pm 0.30 \times 10^{-7}$ m^2/s. The MSD vs t^2 plots [Fig. 14(a)] and D_{Al} values showed that Al diffusion remains largely unaffected in the presence of Sc atoms at 1450 K. In stark contrast, the MSD vs t^2 plots presented in Fig. 14(b) showed significant nonlinear behavior in case of Sc diffusion. It appears that such a behavior is influenced by the presence of cage-like polyhedrons within the liquid phase 0.4 and 1 at.% Sc at 1450 K (Fig. 8). Although, nonlinear MSD vs t^2 plots did not permit extraction of Sc diffusivities, they qualitatively showed that Sc diffusion in between 0.4 and 1 at.% Sc are comparable. This nonlinear behavior can be rationalized on the basis of strong correlation between Sc and surrounding Al atoms that form cage-like structures [see Fig. 10(a)], and the interaction between individual cages [see Fig. 10(b)]. Notwithstanding mechanism of in-liquid atomic movement, our results show that atomic movement in bulk
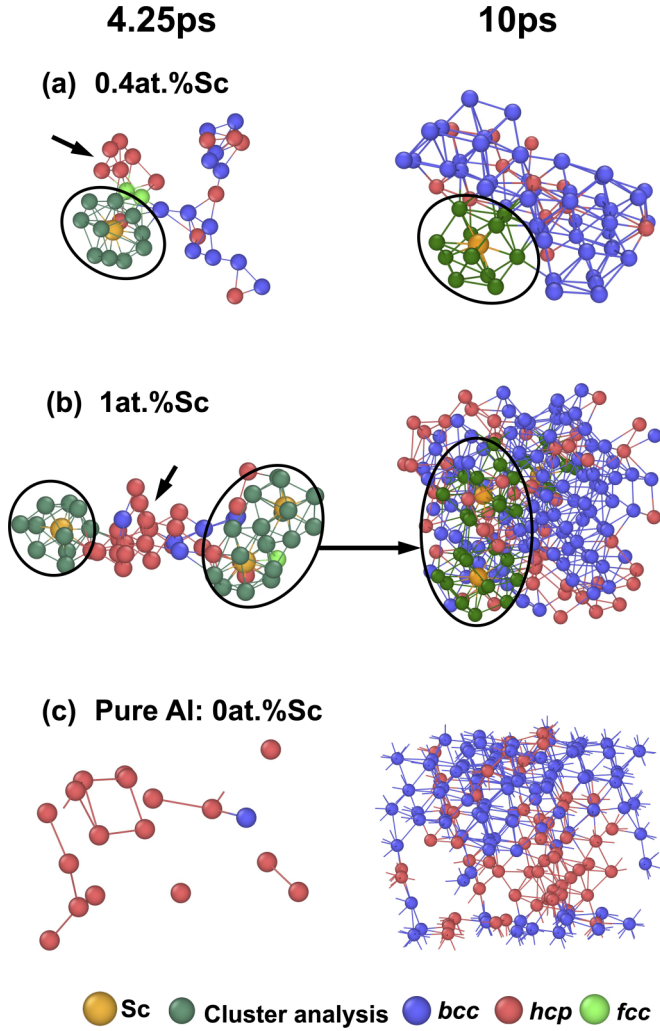
FIG. 13. Sc-centered polyhedron mediated nucleation of metastable *hcp* and *bcc* in 0.4 and 1 at.% Sc alloys at 950 K. AIMD snapshots showing structural evolution after 4.25 and 10 ps of annealing in (a) 0.4 at.% Sc, (b) 1 at.% Sc, and (c) pure Al.
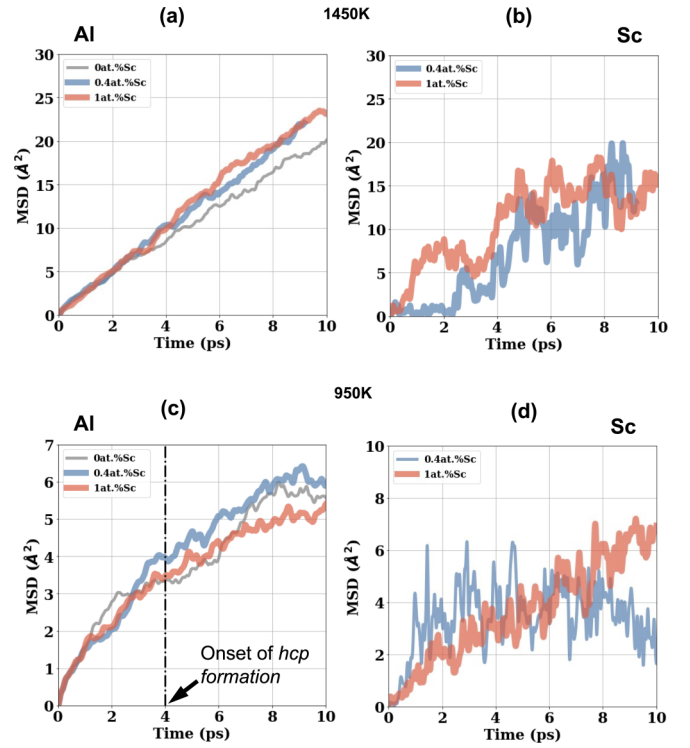

FIG. 14. Comparison of Al and Sc transport properties in 0, 0.4 and 1 at.% Sc. MSD vs t plots showing transport behavior of (a) Al and (b) Sc at 1450 K, and (c) Al and (d) Sc at 950 K.

liquid Al-Sc cannot be described by simple Brownian or random motion alone, rather we must additionally consider effects from strong interatomic correlations exerted by solute species on its immediate neighborhood.

At 950 K, nonlinearity was noted in the MSD vs t^2 plots of both Al [Fig. 14(c)] and Sc [Fig. 14(d)] in all the three systems. Al manifested noticeable nonlinearity after ∼4 ps of annealing [indicated with a dotted line in Fig. 14(c)]. Recall that *hcp* formed within liquid phases after an incubation period of ∼4 ps at 950 K [Fig. 11(b)]. Therefore, it is reasonable that *hcp*-related interatomic correlations have triggered nonlinear behavior in Al after ∼4 ps. We also note that MSD vs t^2 plots for 0.4 and 1 at.% Sc are comparable to pure Al (despite nonlinear behavior), which indicated that Al movement remained unaffected by Sc content at 950 K, at least within ∼4 ps of annealing. In case of Sc, it was rather difficult to examine its behavior due to two sources of nonlinearity: presence of individual and interconnected cages during the incubation period of ∼4 ps [comparable to 1450 K, Fig. 14(a)], and subsequent cage-mediated *hcp* and *bcc* formation (see Fig. 13 and Sec. III C 1). Combined, results

from 950 and 1450 K show that Al movement within liquid phase is independent of solute content (at least up to 1 at.% Sc), while Sc movement is inextricably linked to strong interatomic correlations within liquid phase, i.e., local ordering and crystallization.

IV. DISCUSSION

Our AIMD computations and unsupervised learning-based analysis of simulation results revealed two types of ordered structures within the liquid phase of Al-Sc alloys: First, Al-based ordered layers comprising distorted square motifs and located at the liquid-Al/L1$_2$-Al$_3$Sc interface. Second, Sc-centered polyhedrons with Al-cages that were present in the bulk-liquid domains of 0.4 and 1 at.% Sc alloys. Both in-liquid ordered structures dynamically interacted with their respective environments during annealing at 1450 K; they continually exchanged Al atoms with the surrounding liquid, while maintaining their geometric integrity. However, they crystallized different structures during annealing at a lower temperature of 950 K. The ordered layers at the liquid-Al/L1$_2$-Al$_3$Sc interface heterogeneously nucleated equilibrium *fcc*-Al, while the polyhedrons in 0.4 and 1 at.% Sc facilitated metastable *hcp*- and *bcc*-Al formation. Herein, we will discuss factors contributing to the geometric persistence of in-liquid ordered structures, their influence on crystallization and interaction with the surrounding liquid; and, postulate phase-transformation pathways during the solidification of Al-Sc alloys by using our AIMD results and extant literature.
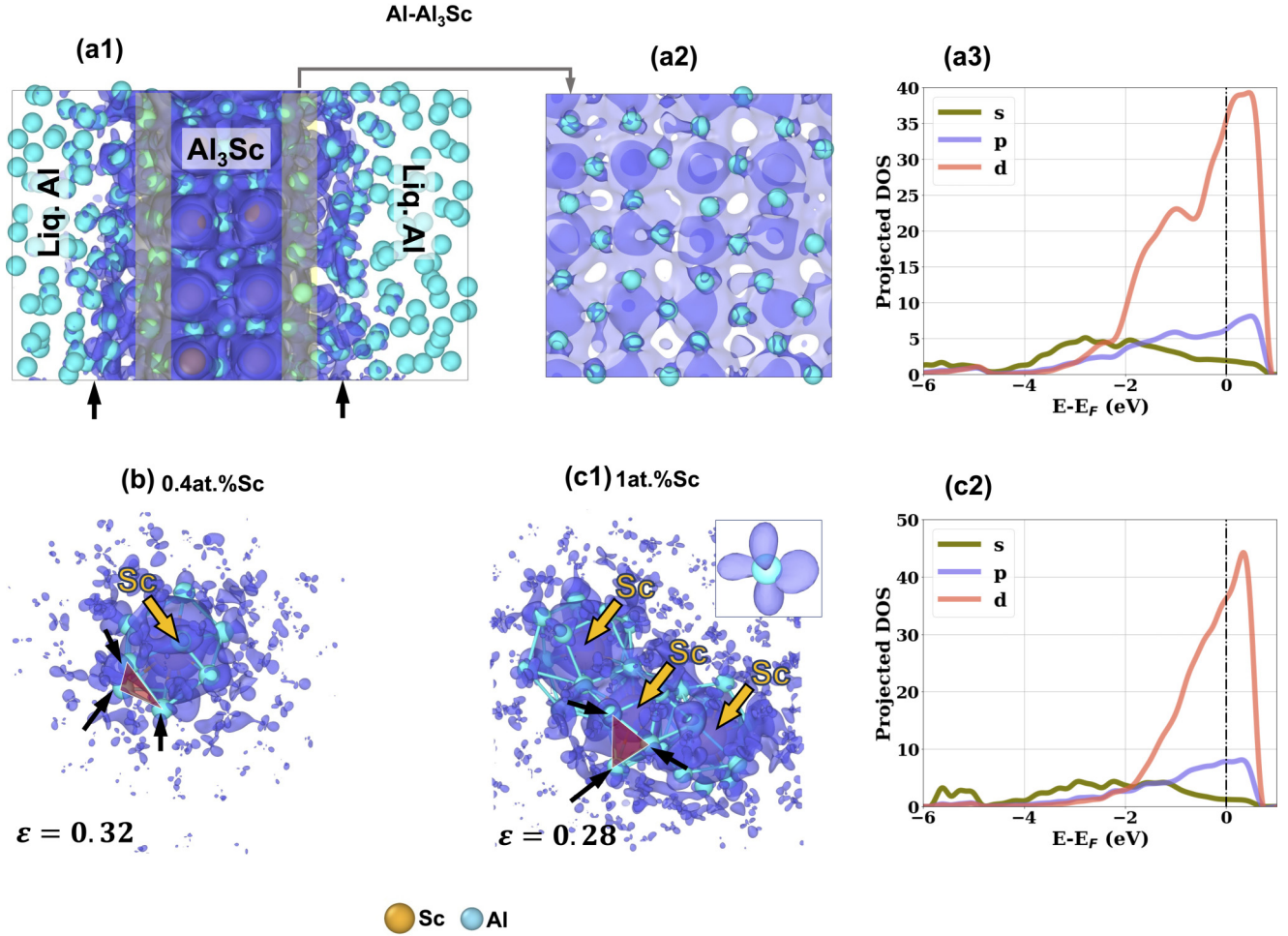
FIG. 15. Bonding character of in-liquid ordered structures after 50 ps of annealing at 1450 K. Panels showing excess electronic charge density within (a1) liquid-Al/L1$_2$-Al$_3$Sc supercell, (a2) an $\{100\}_{fcc-A}$ interfacial ordered layer. (a3) partial density of states (PDOS) plot extracted from the Al atoms in the ordered layer, and shows the electron occupancy in s, p, and d orbitals. Excess electronic charge densities around (b) an isolated Sc-centered polyhedron in 0.4 at.% Sc, and (c1) interconnected polyhedrons in 1 at.% Sc. (c2) PDOS plot extracted from the Al atoms in the interconnected polyhedrons in 1 at.% Sc.

A. Characteristics of interfacial layers and polyhedrons at 1450 K

The formation of interfacial layers and polyhedrons at 1450 K was investigated by examining their bonding character. Towards that end, we first computed electron charge density differences ($\Delta\rho_{1450\,K}$) in liquid-Al/L1$_2$-Al$_3$Sc, and 0.4 and 1 at.% Sc using [92],

$$\Delta\rho_{1450} = \rho_{1450}^{\text{Al-Sc}} - \rho_{1450}^{\text{Al}}, \tag{4}$$

where $\rho_{1450}^{\text{Al-Sc}}$ and $\rho_{1450}^{\text{Al-Sc}}$ are the charge densities of the original supercells and those obtained after replacing Sc with Al, respectively. Here, $\Delta\rho_{1450\,K}$ was computed for structures obtained after 50 ps of annealing at 1450 K. Figures 15(a1), 15(b), and 15(c) show the charge concentrations using $\Delta\rho_{1450\,K} = 2\times10^{-4}$ Å^{-3} isocharge surfaces in liquid-Al/L1$_2$-Al$_3$Sc, 0.4 and 1 at.% Sc supercells, respectively. In Figs. 15(b) and 15(c), liquid atoms were removed for clarity.

Figure 15(a1) qualitatively shows that electron charge localization is highest within L1$_2$-Al$_3$Sc, and such excess charge

density reduces towards the liquid domain. Inside the interfacial layers [also indicated with boxes in Fig. 15(a1)], Al atoms were immersed within a near-homogeneous distribution of charge density [Fig. 15(a2)]. Since the charge density extends from L1$_2$-Al$_3$Sc, Fig. 15(a1) and 15(a2) indicates that the interfacial ordered layer is well bonded to L1$_2$-Al$_3$Sc (compared to liquid Al), and contributed to its geometric stability at 1450 K. Consequently, the interfacial layer acquires the $\{100\}$ or $\{200\}$ crystallography of L1$_2$-Al$_3$Sc [see Figs. 5(a) and 5(b)]. A closer inspection of the interfacial regions in Fig. 15(a1) also indicated the presence of excess charge densities with liquid-Al (marked with black arrows). Such excess charge localization can trap Al atoms by bonding with them at lower temperatures, and form $\{100\}_{fcc}$ planes of Al. This mechanism rationalizes the observed heteroepitaxial nucleation of stable fcc-Al phase during annealing at 950 K (Fig. 12).

Figures 15(b) and 15(c1) show excess charge surrounding Sc-centered polyhedrons. (Sc atoms are marked with arrows, while the Al-based cages are indicated using blue colored bonds.) It may be emphasized that the positional

correspondence between UL-determined polyhedrons, and independently computed charge localization corroborates our methodology for identifying such in-liquid ordered structures (see Secs. II B and III B). The high localization of excess electrons is also indicative of strong Sc-Al and Al-Al bonds within the polyhedrons (compared to the surrounding liquid Al), which also stabilized those cage-like structures at 1450 K. Furthermore, the Sc-Al bonds within the interconnected polyhedrons may have introduced nonlinearity in Sc diffusion by retarding random movement, and preventing it from influencing the movement of Al (Fig. 14 and Sec. III D). It is worth mentioning that bonding related restriction of atomic movement have been reported in the liquid and crystalline phases of Al and Mg-based alloys, respectively [36,93–95].

In Figs. 15(b) and 15(c1), we also note regions with excess charge densities near the surface of polyhedrons. They comprise atoms on the triangular facets of the polyhedrons [marked with a shaded triangle and an black colored arrows in Figs. 15(b) and 15(c1)], and neighboring liquid atoms [inset Fig. 15(c1)]. It is possible that bonding between those regions will promote crystallization at lower temperatures, where the triangular facets will act as "heterogeneous" sites. Classical MD simulations and phase-field crystal (a type of mean-field theory [67,96]) modeling of nucleation in pure metals suggested that triangular symmetries are the fundamental building blocks for *hcp* and *bcc* structures [6,19,97–99]. (The mean-field theories also showed that square motifs facilitate *fcc* formation [100], consistent with our AIMD results, Fig. 5). Therefore, it is likely that the triangular facets initially assisted *hcp* nucleation seen in Figs. 13(a) and 13(b); prior to *bcc* formation [Figs. 11(b) and 11(c)]. It should be noted that *hcp* also formed first in pure Al [Figs. 10(b), 10(c), and 12(c)], which indicated that *hcp* formation is thermodynamically driven. However, our AIMD results indicated the presence of interconnected polyhedrons in 1 at.% Sc enhanced *hcp* formation [Fig. 11(b)]. This suggested that local geometric environment formed by the facets on interconnected polyhedrons may have enhanced *hcp* formation. The effect of such triangular facets on the thermodynamics of *hcp* formation is under investigation. Regardless, the *hcp* domains latter facilitates *bcc* formation in all the systems examined (Figs. 11 and 13).

Focusing on Al-based interfacial ordered structure and polyhedrons, we have also examined their projected density of states (PDOS) to better understand their geometric stability and interactions with the surrounding liquid at 1450 K. Figures 15(a3) and 15(c2) plots their s, p, and d orbital occupancy as function of $E - E_F$, where E_F is the Fermi energy level (indicated with a dotted line). (PDOS of individual polyhedron was comparable to interconnected polyhedra.) Regardless of minor differences, both plots shared two key features. First, they showed nonzero E_F occupancy, which is indicative of metallic bond character [101,102]. This explains the immersion of such structures within a near-homogeneous distribution of electron density—see Figs. 15(a2), 15(b), and 15(c1). Second, in these plots, overlapping of s, p, and d occupancies for all $E - E_F < 0$ suggested hybridization between s, $p,$ and d orbitals—an indicator for covalent bonding [94,95,103,104]. Therefore, interfacial ordered structure and polyhedral cages have a mixed metallic and covalent

character. The stronger [92,94,101] covalent bonds imparts geometric stability to the structures at 1450 K, while the relatively weaker [92,94,101] metallic bonds allowed them to exchange Al atoms with the surrounding liquid.

B. Solidification behavior of Al-Sc alloys

We have also evaluated transformation pathways during the Al-Sc solidification within the context of two categories of literature: experimental studies on effect of Sc additions and L1$_2$-Al$_3$Sc on *fcc*-Al nucleation [14,26–29]; and, fundamental studies showing *bcc*-mediated *fcc* nucleation [15,16,86–90,105].

Microstructural characterization of as-cast and selective laser melted Al-based alloys have shown that Sc is a *potent grain refiner*, and the extent to which grain size reduction can be controlled by changing solute concentration [26–29]. Using transmission electron microscopy, Spierings *et al.* determined that such refinement was facilitated by L1$_2$-Al$_3$Sc mediated nucleation of *fcc*-Al grains [28]. They found that L1$_2$-Al$_3$Sc have a cube-on-cube orientation relationship with *fcc*-Al, which correlates well with our AIMD simulations involving liquid-Al/L1$_2$-Al$_3$Sc (see Fig. 12). However, these studies did not examine the formation of L1$_2$-Al$_3$Sc itself. Recently, using *in situ* synchrotron x-ray diffraction, Huang *et al.* demonstrated the presence of Sc-centered polyhedrons in Al-0.4 at.% Sc, which were precursors for L1$_2$-Al$_3$Sc formation [14]. Such experimentally derived Sc-centered polyhedrons were markedly similar to those observed in our AIMD simulations [see Figs. 8(a2) and 8(b2)]. Time-scale limitations inherent to AIMD did not permit us to examine L1$_2$-Al$_3$Sc formation from such polyhedrons. Regardless, these experimental observations, together with our AIMD results, allowed us to postulate a transformation pathway, involving L1$_2$-Al$_3$Sc-mediated heterogeneous nucleation of *fcc*-Al,

$$In-liquid\ Sc-centered\ polyhedrons \rightarrow Al_3Sc$$
$$\rightarrow \{100\}_{fcc-Al}\ interfacial\ ordering \rightarrow fcc-Al. \quad (5)$$

Furthermore, our AIMD simulations showed that the Sc-centered polyhedrons sequentially formed metastable *hcp*- and *bcc*-Al structures within liquid phase, where *bcc* had a higher volume fraction than *hcp*. However, detailed computational [16,86–90] and experimental [15,105] studies have shown that *bcc* facilitates the nucleation of *fcc* structure (Figs. 10 and 12). Based on these reports and our AIMD results, we can postulate another transformation pathway leading to the homogeneous nucleation of *fcc*-Al,

$$In-liquid\ Sc-centered\ polyhedrons \rightarrow hcp-Al$$
$$\rightarrow bcc-Al \rightarrow fcc-Al, \quad (6)$$

where, *hcp*- and *bcc*-Al constitute the early states of *fcc*-Al nucleation. Thus, Sc-centered polyhedrons can potentially trigger two transformation pathways that cause heterogeneous [Eq. (5)] and homogeneous [Eq. (6)] nucleation of *fcc*-Al during Al-Sc solidification. Few comments are required regarding the implication of our findings.

Notionally, alloy compositions that enhances in-liquid polyhedron population will increase *fcc*-Al nucleation rate and result in a refined solidified microstructure. Our AIMD

simulations indicated that hypereutectic compositions are better suited for that purpose, e.g., see phase diagram in Fig. 1. A similar strategy for designing Al-Sc-based alloys can be deduced on the basis of extensive experimental observations [26,28]. Furthermore, Sc is a rare earth element, whose availability is determined by limited natural resources [106]. Therefore, from an alloy design standpoint, it is prudent to find alternatives for substituting Sc, at least partially, in Al-Sc-based alloys. Solute-centered polyhedrons and intermetallic compound mediated interfacial ordering can be utilized as "design metric", because they facilitate fcc-Al nucleation in Al-Sc alloys. Elements that produce comparable in-liquid ordering may serve as potential substitutes.

Broadly, our results provide insights into engineering the solidification behavior alloys starting from the liquid melt, i.e., liquid-phase engineering of alloys. This approach may prove useful for selecting alloys that are fabricated using laser based additive manufacturing (AM), e.g., laser powder bed fusion (LPBF) or directed energy deposition (DED) [107,108]. Particularly, when conventional alloys do not produce reliable AM printed parts [107,108]. Therefore, the controlling nucleation mechanisms within small melt pools, produced during DED-AM, may determine whether the final solidified microstructure is dendritic or fine grained [28,29,108–110].
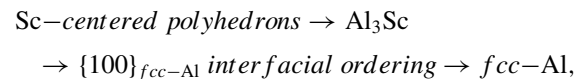
V. SUMMARY

Ab inito molecular dynamics (AIMD) was employed to investigate the effect of Sc content and intermetallic L1$_2$-Al$_3$Sc on the liquid phase ordering in Al-Sc alloys at 1450 K, and nucleation at 950 K. The AIMD simulations probed structural changes in three bulk compositions, i.e., Al-xSc ($x = 0, 0.4, 1.0$ at.%), and regions near the liquid-Al/Al$_3$Sc interface. Ordered structures within liquid state were determined using unsupervised learning techniques, which included structural fingerprinting, dimensionality reduction, and cluster analysis. Our main findings are as follows:
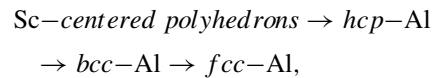
(1) Two types of ordered structures were observed within the liquid phase of Al-Sc at 1450 K. Lower Sc content, i.e., 0.4 at.%, formed Sc-centered polyhedrons, which roughly resembled distorted icosahedrons. At higher Sc concentrations, i.e., 1 at.%, interconnected Sc-centered polyhedrons were observed. Planar ordering was noted at the liquid-Al/Al$_3$Sc interface that was comparable to {100} planes of fcc structure. The outer cage of the Sc-centered polyhedra and the {100} interfacial plane were comprised of Al atoms.

(2) Both ordered structures exchanged Al atoms with the surrounding liquid, while retaining their geometric integrity at 1450 K, i.e., they were structurally persistent, but constitutionally transient or emergent. This behavior was rationalized on the basis of their mixed metallic and covalent bond character. Strong Sc-Al bonds in the Sc-centered polyhedrons caused non-Brownian movement of Sc atoms within liquid, which manifested as a nonlinearity in its mean squared displacement *v.s.* time plots. Interestingly, Sc did not influence the diffusion of liquid Al atoms, which experienced the expected Brownian motion.

(3) The two types of in-liquid ordering facilitated in the nucleation of different structures after annealing at 950 K. The {100}$_{Al_3Sc}$ interfacial plane promoted heteroepitaxial nucleation of equilibrium fcc-Al phase. This nucleated phase shared a cube-on-cube orientation relationship with L1$_2$-Al$_3$Sc, i.e., $\langle 001 \rangle_{fcc}$ // $\langle 001 \rangle_{Al_3Sc}$. In contrast, the Sc-centered polyhedrons sequentially nucleated metastable hcp- and bcc-Al. These two phases presumably constituted the early stages of nucleation of fcc-Al. Our AIMD results and extant literature allowed us to postulate two possible pathways for the transformation of in-liquid ordered structures into equilibrium fcc.

$$Sc-centered\ polyhedrons \rightarrow Al_3Sc$$
$$\rightarrow \{100\}_{fcc-Al}\ interfacial\ ordering \rightarrow fcc-Al,$$

and

$$Sc-centered\ polyhedrons \rightarrow hcp-Al$$
$$\rightarrow bcc-Al \rightarrow fcc-Al,$$

(4) The formation of Sc-centered polyhedrons and {100} interfacial ordering within liquid Al-Sc alloys provided an atomistic basis for Sc element as a potent grain refiner, and also, serve as possible structural metrics for designing novel alloys.

ACKNOWLEDGMENTS

[1] M. Saboungi, W. Geertsma, and D. Price, Ordering in liquid alloys, Annu. Rev. Phys. Chem. **41**, 207 (1990).

[2] D. Holland-Moritz, Short-range order and solid–liquid interfaces in undercooled metallic melts, Mater. Sci. Eng. A **304–306**, 108 (2001).

[3] G. Lee, A. Gangopadhyay, T. Croat, T. Rathz, R. Hyers, J. Rogers, and K. Kelton, Link between liquid structure and the nucleation barrier for icosahedral quasicrystal, polytetrahedral, and simple crystalline phases in Ti-Zr-Ni alloys: Verification of Frank's hypothesis, Phys. Rev. B **72**, 174107 (2005).

[4] G. Kurtuldu, P. Jarry, and M. Rappaz, Influence of Cr on the nucleation of primary al and formation of twinned dendrites in Al–Zn–Cr alloys: Can icosahedral solid clusters play a role?, Acta Mater. **61**, 7098 (2013).

[5] Y. Zhang, H. Zheng, Y. Liu, L. Shi, R. Xu, and X. Tian, Cluster-assisted nucleation of silicon phase in hypoeutectic Al–Si alloy with further inoculation, Acta Mater. **70**, 162 (2014).

[6] D. Choudhuri and B. S. Majumdar, Structural changes during crystallization and vitrification of dilute fcc-based binary Alloys, Materialia **12**, 100816 (2020).

[7] S. Cao, L. Zeng, M. Xia, N. Jakse, P. Yu, W. Lu, and J. Li, Icosahedral ordering induced by Cr in Al–Zn alloy liquid, Metall. Mater. Trans. A **53**, 3274 (2022).

[8] S. Wang, M. Kramer, M. Xu, S. Wu, S. Hao, D. Sordelet, K. Ho, and C. Wang, Experimental and *ab initio* molecular dynamics simulation studies of liquid $Al_{60}Cu_{40}$ alloy, Phys. Rev. B **79**, 144205 (2009).

[9] L. Xiong, F. Guo, X. Wang, Q. Cao, D. Zhang, Y. Ren, and J. Jiang, Structural evolution and dynamical properties of Al_2Ag and Al_2Cu liquids studied by experiments and *ab initio* molecular dynamics simulations, J. Non-Cryst. Solids **459**, 160 (2017).

[10] P. Jarry and M. Rappaz, Recent advances in the metallurgy of aluminium alloys. Part I: Solidification and casting, C. R. Phys. **19**, 672 (2018).

[11] Z. Ye, F. Meng, F. Zhang, Y. Sun, L. Yang, S. Zhou, R. Napolitano, M. Mendelev, R. Ott, M. Kramer *et al.*, Observation of η-$Al_{41}Sm_5$ reveals motif-aware structural evolution in Al-Sm alloys, Sci. Rep. **9**, 6692 (2019).

[12] J. You, C. Wang, S.-L. Shang, Y. Gao, H. Ju, H. Ning, Y. Wang, H.-Y. Wang, and Z.-K. Liu, Ordering in liquid and its heredity impact on phase transformation of Mg-Al-Ca alloys, J. Magnes. Alloys (in press), https://doi.org/10.1016/j.jma.2021.11.024.

[13] J. Ma, S.-L. Shang, H. Kim, and Z.-K. Liu, An *ab initio* molecular dynamics exploration of associates in Ba-Bi liquid with strong ordering trends, Acta Mater. **190**, 81 (2020).

[14] S. Huang, S. Luo, L. Qin, D. Shu, B. Sun, A. J. Lunt, A. M. Korsunsky, and J. Mi, 3D local atomic structure evolution in a solidifying Al-0.4Sc dilute alloy melt revealed in operando by synchrotron x-ray total scattering and modelling, Scr. Mater. **211**, 114484 (2022).

[15] R. Cech, Undercooling of Fe-Ni droplets, Trans. Metall. AIME **206**, 585 (1956).

[16] P. R. Ten Wolde, M. J. Ruiz-Montero, and D. Frenkel, Numerical Evidence for bcc Ordering at the Surface of a Critical fcc Nucleus, Phys. Rev. Lett. **75**, 2714 (1995).

[17] M. Mandell, J. McTague, and A. Rahman, Crystal nucleation in a three-dimensional Lennard-Jones system. II. Nucleation kinetics for 256 and 500 particles, J. Chem. Phys. **66**, 3070 (1977).

[18] W. C. Swope and H. C. Andersen, 10^6-particle molecular-dynamics study of homogeneous nucleation of crystals in a supercooled atomic liquid, Phys. Rev. B **41**, 7042 (1990).

[19] F. Cherne, M. Baskes, R. Schwarz, S. Srinivasan, and W. Klein, Non-classical nucleation in supercooled nickel, Modell. Simul. Mater. Sci. Eng. **12**, 1063 (2004).

[20] C. Desgranges and J. Delhommelle, Molecular mechanism for the cross-nucleation between polymorphs, J. Am. Chem. Soc. **128**, 10368 (2006).

[21] H. Wang, H. Gould, and W. Klein, Homogeneous and heterogeneous nucleation of Lennard-Jones liquids, Phys. Rev. E **76**, 031604 (2007).

[22] S. Orihara, Y. Shibuta, and T. Mohri, Molecular dynamics simulation of nucleation from undercooled melt of nickel–aluminum alloy and discussion on polymorphism in nucleation, Mater. Trans. **61**, 750 (2020).

[23] D. Choudhuri, S. Matteson, and R. Knox, Nucleation of coupled body-centered-cubic and closed-packed struc-

[24] D. N. Seidman, E. A. Marquis, and D. C. Dunand, Precipitation strengthening at ambient and elevated temperatures of heat-treatable Al(Sc) alloys, Acta Mater. **50**, 4021 (2002).

[25] E. A. Marquis, D. N. Seidman, and D. C. Dunand, Effect of Mg addition on the creep and yield behavior of an Al–Sc alloy, Acta Mater. **51**, 4751 (2003).

[26] A. Norman, P. Prangnell, and R. McEwen, The solidification behaviour of dilute aluminium–scandium alloys, Acta Mater. **46**, 5715 (1998).

[27] S. Costa, H. Puga, J. Barbosa, and A. Pinto, The effect of Sc additions on the microstructure and age hardening behaviour of as cast Al–Sc alloys, Mater. Des. **42**, 347 (2012).

[28] A. B. Spierings, K. Dawson, T. Heeling, P. J. Uggowitzer, R. Schäublin, F. Palm, and K. Wegener, Microstructural features of Sc-and Zr-modified Al-Mg alloys processed by selective laser melting, Mater. Des. **115**, 52 (2017).

[29] K. V. Yang, Y. Shi, F. Palm, X. Wu, and P. Rometsch, Columnar to equiaxed transition in Al-Mg(-Sc)-Zr alloys produced by selective laser melting, Scr. Mater. **145**, 113 (2018).

[30] C. Fang and Z. Fan, Ab Initio Molecular Dynamics Investigation of Prenucleation at Liquid-Metal/Oxide Interfaces: An Overview, Metals **12**(10), 1618 (2022).

[31] S. H. Oh, Y. Kauffmann, C. Scheu, W. D. Kaplan, and M. Ruhle, Ordered liquid aluminum at the interface with sapphire, Science **310**, 661 (2005).

[32] S. Becker, E. Devijver, R. Molinier, and N. Jakse, Unsupervised topological learning approach of crystal nucleation, Sci. Rep. **12**, 3195 (2022).

[33] J. Boyce, S. Benson, C. Bohn, D. Douglas, H. Dylla, J. Gubeli, U. Happek, K. Jordan, G. Krafft, G. Neil *et al.*, The Jefferson lab sub-picosecond x-ray program, AIP Conf. Proc. **680**, 325 (2003).

[34] K. R. Ferguson, M. Bucher, J. D. Bozek, S. Carron, J.-C. Castagna, R. Coffee, G. I. Curiel, M. Holmes, J. Krzywinski, M. Messerschmidt *et al.*, The atomic, molecular and optical science instrument at the linac coherent light source, J. Synchrotron Radiat. **22**, 492 (2015).

[35] M. P. Allen and D. J. Tildesley, *Computer Simulation of Liquids* (Oxford University Press, Oxford, 2017).

[36] N. Jakse and A. Pasturel, Transport properties and stokes-einstein relation in al-rich liquid alloys, J. Chem. Phys. **144**, 244502 (2016).

[37] A. Pasturel and N. Jakse, Influence of Cr on local order and dynamic properties of liquid and undercooled Al–Zn alloys, J. Chem. Phys. **146**, 184502 (2017).

[38] C. Fang and Z. Fan, Atomic ordering at the liquid-$Al/MgAl_2O_4$ interfaces from *ab initio* molecular dynamics simulations, Metall. Mater. Trans. A **51**, 6318 (2020).

[39] C. Fang and Z. Fan, Prenucleation at the interface between mgo and liquid magnesium: An *ab initio* molecular dynamics study, Metall. Mater. Trans. A **51**, 788 (2020).

[40] P. J. Steinhardt, D. R. Nelson, and M. Ronchetti, Bond-orientational order in liquids and glasses, Phys. Rev. B **28**, 784 (1983).

[41] W. Lechner and C. Dellago, Accurate determination of crystal structures based on averaged local bond order parameters, J. Chem. Phys. **129**, 114707 (2008).

[42] H. Tsuzuki, P. S. Branicio, and J. P. Rino, Structural characterization of deformed crystals by analysis of common atomic neighborhood, Comput. Phys. Commun. **177**, 518 (2007).

[43] Y. Cheng and E. Ma, Atomic-level structure and structure–property relationship in metallic glasses, Prog. Mater. Sci. **56**, 379 (2011).

[44] P. M. Larsen, S. Schmidt, and J. Schiøtz, Robust structural identification via polyhedral template matching, Modell. Simul. Mater. Sci. Eng. **24**, 055007 (2016).

[45] R. Jadrich, B. Lindquist, and T. Truskett, Unsupervised machine learning for detection of phase transitions in off-lattice systems. I. Foundations, J. Chem. Phys. **149**, 194109 (2018).

[46] T. Xie, A. France-Lanord, Y. Wang, Y. Shao-Horn, and J. C. Grossman, Graph dynamical networks for unsupervised learning of atomic scale dynamics in materials, Nat. Commun. **10**, 2667 (2019).

[47] J. Schmidt, M. R. Marques, S. Botti, and M. A. Marques, Recent advances and applications of machine learning in solid-state materials science, npj Comput. Mater. **5**, 83 (2019).

[48] C. S. Adorf, T. C. Moore, Y. J. Melle, and S. C. Glotzer, Analysis of self-assembly pathways with unsupervised machine learning algorithms, J. Phys. Chem. B **124**, 69 (2020).

[49] R. Wang, Y.-G. Ma, R. Wada, L.-W. Chen, W.-B. He, H.-L. Liu, and K.-J. Sun, Nuclear liquid-gas phase transition with machine learning, Phys. Rev. Res. **2**, 043202 (2020).

[50] G. E. Hinton and S. Roweis, Stochastic neighbor embedding, in advances in neural information processing systems, Vol. 15 (2002).

[51] B. L. DeCost, T. Francis, and E. A. Holm, Exploring the microstructure manifold: Image texture representations applied to ultrahigh carbon steel microstructures, Acta Mater. **133**, 30 (2017).

[52] D. P. Kingma and M. Welling, An introduction to variational autoencoders, Found. Trends Mach. Learn. **12**, 307 (2019).

[53] E. A. Holm, R. Cohn, N. Gao, A. R. Kitahara, T. P. Matson, B. Lei, and S. R. Yarasi, Overview: Computer vision and machine learning for microstructural characterization and analysis, Metall. Mater. Trans. A **51**, 5985 (2020).

[54] C. D. Taylor and B. M. Tossey, High temperature oxidation of corrosion resistant alloys from machine learning, npj Mater. Degrad. **5**, 38 (2021).

[55] T. Kirk, B. Vela, S. Mehalic, K. Youssef, and R. Arróyave, Entropy-driven melting point depression in fcc heas, Scr. Mater. **208**, 114336 (2022).

[56] M. Ester, H.-P. Kriegel, J. Sander, and X. Xu, A density-based algorithm for discovering clusters in large spatial databases with noise, in *KDD'96: Proceedings of the Second International Conference on Knowledge Discovery and Data Mining*, Vol. 96 (1996) pp. 226–231.

[57] R. Marceau, L. Stephenson, C. Hutchinson, and S. Ringer, Quantitative atom probe analysis of nanostructure containing clusters and precipitates with multiple length scales, Ultramicroscopy **111**, 738 (2011).

[58] G.-G. Lee, H.-H. Jin, K. Chang, S. Lim, M.-C. Kim, B.-S. Lee, and J. Kwon, Atom probe tomography analysis of nanostructure evolution in Ni-Cr-Mo low alloy steel under neutron irradiation, J. Mech. Sci. Tech. **31**, 3675 (2017).

[59] A. Kwiatkowski da Silva, D. Ponge, Z. Peng, G. Inden, Y. Lu, A. Breen, B. Gault, and D. Raabe, Phase nucleation through confined spinodal fluctuations at crystal defects evidenced in Fe-Mn alloys, Nat. Commun. **9**, 1137 (2018).

[60] A. J. Parker and A. S. Barnard, Selecting appropriate clustering methods for materials science applications of machine learning, Adv. Theory Simul. **2**, 1900145 (2019).

[61] M. P. Deisenroth, A. A. Faisal, and C. S. Ong, *Mathematics for Machine Learning* (Cambridge University Press, Cambridge, 2020).

[62] G. Kresse and J. Hafner, Ab initio molecular dynamics for liquid metals, Phys. Rev. B **47**, 558 (1993).

[63] G. Kresse and J. Hafner, *Ab initio* molecular-dynamics simulation of the liquid-metal–amorphous-semiconductor transition in germanium, Phys. Rev. B **49**, 14251 (1994).

[64] G. Kresse and J. Furthmüller, Efficiency of *ab-initio* total energy calculations for metals and semiconductors using a plane-wave basis set, Comput. Mater. Sci. **6**, 15 (1996).

[65] G. Kresse and D. Joubert, From ultrasoft pseudopotentials to the projector augmented-wave method, Phys. Rev. B **59**, 1758 (1999).

[66] J. Murray, The Al-Sc (aluminum-scandium) system, J. Phase Equilibria and Diffus. **19**, 380 (1998).

[67] P. M. Chaikin and Lubensky, *Principles of Condensed Matter Physics* (Cambridge University Press, Cambridge, 1995).

[68] K. Ueno and Y. Shibuta, Composition dependence of solid-liquid interfacial energy of Fe-Cr binary alloy from molecular dynamics simulations, Comput. Mater. Sci. **167**, 1 (2019).

[69] E. Kirova and V. Pisarev, System size effect on crystal nuclei morphology in supercooled metallic melt, J. Cryst. Growth **528**, 125266 (2019).

[70] K. Ueno and Y. Shibuta, Molecular dynamics study of composition dependence of solid-liquid interfacial energy of fe-ni binary alloy, in *IOP Conference Series: Materials Science and Engineering* (IOP Publishing, Bristol, 2020), Vol. 861, p. 012064.

[71] T. Fukuya and Y. Shibuta, Machine learning approach to automated analysis of atomic configuration of molecular dynamics simulation, Comput. Mater. Sci. **184**, 109880 (2020).

[72] See Supplemental Material at http://link.aps.org/supplemental/10.1103/PhysRevMaterials.6.103406 for additional formula and figures.

[73] A. Stukowski, Visualization and analysis of atomistic simulation data with OVITO–the open Visualization Tool, Modell. Simul. Mater. Sci. Eng. **18**, 015012 (2010).

[74] D. Buta, M. Asta, and J. J. Hoyt, Atomistic simulation study of the structure and dynamics of a faceted crystal-melt interface, Phys. Rev. E **78**, 031605 (2008).

[75] M. Mendelev, M. Asta, M. Rahman, and J. Hoyt, Development of interatomic potentials appropriate for simulation of solid–liquid interface properties in Al–Mg alloys, Philos. Mag. **89**, 3269 (2009).

[76] L. Wang and J. J. Hoyt, Layering misalignment and negative temperature dependence of interfacial free energy of B2-liquid interfaces in a glass forming system, Acta Mater. **219**, 117259 (2021).

[77] J. M. Haile, *Molecular Dynamics Simulation: Elementary Methods* (John Wiley & Sons, Hoboken, NJ, 1992).

[78] A. P. Bartók, R. Kondor, and G. Csányi, On representing chemical environments, Phys. Rev. B **87**, 184115 (2013).

[79] S. De, A. P. Bartók, G. Csányi, and M. Ceriotti, Comparing molecules and solids across structural and alchemical space, Phys. Chem. Chem. Phys. **18**, 13754 (2016).

[80] M. Kühbach, P. Bajaj, H. Zhao, M. H. Çelik, E. A. Jägle, and B. Gault, On strong-scaling and open-source tools for analyzing atom probe tomography data, npj Comput. Mater. **7**, 21 (2021).

[81] D. Chakravarty, N. Laxman, R. Jayasree, R. Mane, S. Mathiazhagan, P. Srinivas, R. Das, M. Nagini, M. Eizadjou, L. Venkatesh *et al.*, Ultrahigh transverse rupture strength in tungsten-based nanocomposites with minimal lattice misfit and dual microstructure, Int. J. Refract. Hard Mat. **95**, 105454 (2021).

[82] L. Himanen, M. O. Jäger, E. V. Morooka, F. F. Canova, Y. S. Ranawat, D. Z. Gao, P. Rinke, and A. S. Foster, Dscribe: Library of descriptors for machine learning in materials science, Comput. Phys. Commun. **247**, 106949 (2020).

[83] F. Pedregosa, G. Varoquaux, A. Gramfort, V. Michel, B. Thirion, O. Grisel, M. Blondel, P. Prettenhofer, R. Weiss, V. Dubourg *et al.*, Scikit-learn: Machine learning in python, the J. Mach. Learn. Res. **12**, 2825 (2011).

[84] M. R. P. Elenchezian, V. Vadlamudi, R. Raihan, and K. Reifsnider, Unsupervised learning methods for identification of defects in heterogeneous materials, in *Proceedings of the American Society for Composites-Thirty-fifth Technical Conference* (DEStech Publications, Inc, Lancaster, PA, USA, 2020).

[85] M. Alshammari, J. Stavrakakis, and M. Takatsuka, Refining a k-nearest neighbor graph for a computationally efficient spectral clustering, Pattern Recognit. **114**, 107869 (2021).

[86] S. Alexander and J. McTague, Should All Crystals Be bcc? Landau Theory of Solidification and Crystal Nucleation, Phys. Rev. Lett. **41**, 702 (1978).

[87] B. Groh and B. Mulder, Why all crystals need not be bcc: Symmetry breaking at the liquid-solid transition revisited, Phys. Rev. E **59**, 5613 (1999).

[88] W. Klein and F. Leyvraz, Crystalline Nucleation in Deeply Quenched Liquids, Phys. Rev. Lett. **57**, 2845 (1986).

[89] Y. C. Shen and D. W. Oxtoby, bcc Symmetry in the Crystal-Melt Interface of Lennard-Jones Fluids Examined through Density Functional Theory, Phys. Rev. Lett. **77**, 3585 (1996).

[90] D. W. Oxtoby and Y. C. Shen, Density functional approaches to the dynamics of phase transitions, J. Phys.: Condens. Matter **8**, 9657 (1996).

[91] T. L. Hill, *An Introduction to Statistical Thermodynamics* (Courier Corporation, New York, 1986).

[92] D. Choudhuri, Y. Zheng, T. Alam, R. Shi, M. Hendrickson, S. Banerjee, Y. Wang, S. Srinivasan, H. Fraser, and R. Banerjee, Coupled experimental and computational investigation of omega phase evolution in a high misfit titanium-vanadium alloy, Acta Mater. **130**, 215 (2017).

[93] W. Wang, J. Han, H. Fang, J. Wang, Y. Liang, S. Shang, Y. Wang, X. Liu, L. Kecskes, S. Mathaudhu *et al.*, Anomalous structural dynamics in liquid $Al_{80}Cu_{20}$: An *ab initio* molecular dynamics study, Acta Mater. **97**, 75 (2015).

[94] D. Choudhuri, S. G. Srinivasan, M. A. Gibson, Y. Zheng, D. L. Jaeger, H. L. Fraser, and R. Banerjee, Exceptional increase in the creep life of magnesium rare-earth alloys due to localized bond stiffening, Nat. Commun. **8**, 2000 (2017).

[95] P. Paranjape, S. Srinivasan, and D. Choudhuri, Correlation between bonding, vacancy migration mechanisms, and creep in model binary and ternary hcp-Mg solid solutions, J. Appl. Phys. **128**, 145103 (2020).

[96] N. Provatas and K. Elder, *Phase-Field Methods in Materials Science and Engineering* (John Wiley & Sons, Hoboken, NJ, 2011).

[97] K. R. Elder, N. Provatas, J. Berry, P. Stefanovic, and M. Grant, Phase-field crystal modeling and classical density functional theory of freezing, Phys. Rev. B **75**, 064107 (2007).

[98] G. I. Tóth, G. Tegze, T. Pusztai, G. Tóth, and L. Gránásy, Polymorphism, crystal nucleation and growth in the phase-field crystal model in 2D and 3D, J. Phys.: Condens. Matter **22**, 364101 (2010).

[99] M. Greenwood, J. Rottler, and N. Provatas, Phase-field-crystal methodology for modeling of structural transformations, Phys. Rev. E **83**, 031601 (2011).

[100] K.-A. Wu, A. Adland, and A. Karma, Phase-field-crystal model for fcc ordering, Phys. Rev. E **81**, 061601 (2010).

[101] A. P. Sutton, *Electronic Structure of Materials* (Clarendon Press, Oxford, 1993).

[102] N. W. Ashcroft and N. D. Mermin, Solid state physics (Saunders College, Philadelphia, 1976), Appendix N **166**, 87 (2010).

[103] D. Choudhuri, S. Srinivasan, M. A. Gibson, and R. Banerjee, Bonding environments in a creep–resistant Mg–Re–Zn alloy, in *Magnesium Technology 2017* (Springer, Warrendale, PA, 2017), pp. 471–475.

[104] D. Choudhuri, Local structure and bonding environment of intermetallic $\beta 1$ precipitate phase nucleus in binary Mg-Nd, Comput. Mater. Sci. **187**, 110111 (2021).

[105] T. Volkmann, D. Herlach, and W. Löser, Nucleation and phase selection in undercooled Fe-Cr-Ni melts: Part I. theoretical analysis of nucleation behavior, Metall. Mater. Trans. A **28**, 453 (1997).

[106] A. B. Junior, D. C. R. Espinosa, J. Vaughan, and J. A. S. Tenório, Recovery of scandium from various sources: A critical review of the state of the art and future prospects, Miner. Eng. **172**, 107148 (2021).

[107] L. Zhou, H. Hyer, S. Park, H. Pan, Y. Bai, K. P. Rice, and Y. Sohn, Microstructure and mechanical properties of Zr-modified aluminum alloy 5083 manufactured by laser powder bed fusion, Addit. Manuf. **28**, 485 (2019).

[108] A. Bandyopadhyay, K. D. Traxel, M. Lang, M. Juhasz, N. Eliaz, and S. Bose, Alloy design via additive manufacturing: Advantages, challenges, applications and perspectives, Mater. Today **52**, 207 (2022).

[109] S. Mantri, T. Alam, D. Choudhuri, C. Yannetta, C. Mikler, P. Collins, and R. Banerjee, The effect of boron on the grain size and texture in additively manufactured β-Ti alloys, J. Mater. Sci. **52**, 12455 (2017).

[110] D. Zhang, D. Qiu, M. A. Gibson, Y. Zheng, H. L. Fraser, D. H. StJohn, and M. A. Easton, Additive manufacturing of ultrafine-grained high-strength titanium alloys, Nature (London) **576**, 91 (2019).